Article:
Cao, L, Cochrane, RF and Mullis, AM (2015) Solidification morphology and phase selection in drop-tube processed Ni-Fe-Si intermetallics. Intermetallics, 60. 33 - 44. ISSN 0966-9795

https://doi.org/10.1016/j.intermet.2015.01.006

Solidification morphology and phase selection in drop-tube processed Ni-Fe-Si intermetallics

Leigang Cao[1,a], Robert F Cochrane[1,b] and Andrew M Mullis[1,c]

[1]Institute for Materials Research, University of Leeds, Leeds LS2-9JT, UK.

[a]E-mail address: pmlc@leeds.ac.uk

[b]E-mail address: r.f.cochrane@leeds.ac.uk

[c]Corresponding author: Tel. +44 113 343 2568. Email address: a.m.mullis@leeds.ac.uk

Abstract

Drop-tube processing was used to rapidly solidify droplets of $Ni_{64.7}Fe_{10}Si_{25.3}$ and $Ni_{59.7}Fe_{15}Si_{25.3}$ alloys. In the larger droplets, and therefore at low cooling rates, only two phases, γ-$Ni_{31}Si_{12}$ and β_1-Ni_3Si were observed. Conversely, in the smaller droplets, and therefore at higher cooling rates, the metastable phase $Ni_{25}Si_9$ was also observed. The critical cooling rate for the formation of $Ni_{25}Si_9$ was estimated as 5×10^3 K s^{-1}. SEM and TEM analysis reveals three typical microstructures: (I) a regular structure, comprising single-phase γ-$Ni_{31}Si_{12}$ and a eutectic structure between γ-$Ni_{31}Si_{12}$ and β_1-Ni_3Si; (II) a refined lamellar structure with a lamellar spacing < 50 nm comprising γ-$Ni_{31}Si_{12}$ and β_1-Ni_3Si; (III) an anomalous structure with a matrix of $Ni_{25}Si_9$ and only a very small proportion of a second, and as yet unidentified, phase. These results indicate that there is an extended stability field for $Ni_{25}Si_9$ in the Ni-rich part of the Ni-Fe-Si ternary system in comparison to the Ni-Si binary system. With an increase of cooling rate, an increasing fraction of small droplets experience high undercoolings and, therefore, can be undercooled into the $Ni_{25}Si_9$ stability field forming droplets consisting of only the anomalous structure (III). The Fe atoms are found to occupy different substitutional sites in different phase, i.e. Fe substitutes for Ni in the γ phase and Si in the $L1_2$ (β_1) phase respectively.

Keywords: A. Intermetallics; C. Rapid Solidification; D. Microstructure;

1 Introduction

The solidification of intermetallic compounds such as Ni_3Si, Ni_3Al and Ni_3Fe has attracted significant interest due to their attractive mechanical properties [1]; e.g. β-Ni_3Si displays a high melting point, excellent oxidation resistance and high strength at elevated temperatures. However, like many intermetallics, limited room temperature ductility restricts potential application of these materials due to the difficulty in fabricating engineering components via conventional processing routes [2-5]. One potential route to overcome this difficulty is to form intermetallic-metal matrix composites by incorporating a ductile phase into the brittle matrix, or by solidifying a ductile phase directly from the parent melt, to form a so-called *in-situ* composite [6-8]. Another potential route to improve this lack of formability is non-equilibrium processing via rapid solidification. The resulting refined grain structure [9-11] and the presence of anti-phase domains resulting from the spontaneous ordering, in the solid-state, of initially disordered structures, gives rise to increased room temperature ductility and improved formability [12, 13]. Moreover, in this route, annealing subsequent to forming can restore the desirable high temperature mechanical properties of the intermetallic.

At the Ni-rich end of the Ni-Si phase diagram, which is shown in Fig. 1a, the main phases present are α-Ni and the intermetallics β-Ni_3Si, γ-$Ni_{31}Si_{12}$ and δ-Ni_2Si. The β intermetallics occurs in three forms, a low temperature polymorph, β_1, which has the $L1_2$ crystal structure (space group 221, Pm3m) and two high temperature forms, β_2 (ordered) and β_3 (disordered), both of which have the $D0_{22}$ crystal structure (space group 139, I4/mmm). For completeness, although not shown on the phase diagram, the metastable compound $Ni_{25}Si_9$ can also be observed in Ni-rich Ni-Si alloys at high cooling rate. $Ni_{31}Si_{12}$ and $Ni_{25}Si_9$ are both rhombohederal structures, belonging to space groups 150 (P321) and 147 (P3) respectively. Ni_2Si is not considered further as it is not observed in this investigation.

A number of studies have been carried out into the non-equilibrium solidification of Ni-rich Ni-Si alloys, these being mostly on the eutectic composition, Ni-21.4 at.% Si [14-18]. The focus of these has been to understand the fundamental solidification processes occurring in these alloys. The direct solidification of β-Ni_3Si from a melt of the same composition has been studied by Ahmad et al. [19], who performed undercooling experiments on a Ni-25.3 at.% Si alloy using a melting-fluxing technique. Based on the equilibrium phase diagram, with the γ-liquidus at this composition estimated at 1496 K, direct solidification to primary β should have become possible for undercoolings in excess of 53 K. However, despite obtaining the

required undercooling, Ahmad et al. were unable to obtain single-phase β-Ni_3Si. Instead, at all undercoolings, the solidification was always to a lamellar eutectic structure of single-phase γ-$Ni_{31}Si_{12}$ and an Ni-rich lamellar consisting of a fine, eutectoid dispersion of α-Ni and β_1. In addition, for undercoolings in excess of 132 K small amounts of the high temperature β_3-phase were observed uniformly dispersed throughout the sample. The direct formation of the low temperature β_1-phase direct from the melt was not observed, with the only source of β_1 being the eutectoid decomposition of the supersaturated solid solution noted above. The measured growth velocities were extremely low, with a maximum of 0.018 m s^{-1} being observed at the maximum undercooling of 160 K. This is consistent with the general trend revealed by previous studies on Ni-Si alloys, namely that the solidification velocity drops with increasing Si concentration [20, 21]. Ahmad et al. also noted an exceptionally high apparent viscosity in the melt and a general resistance to nucleation of the melt, both of which they attributed to Si acting as a network former in the melt at this composition. In addition, small amounts of the metastable phases $Ni_{25}Si_9$ were retained in the as-solidified structure, despite the low cooling rate, estimated as < 10 K s^{-1}.

Recently, Cao et al. [22-24] have extended the study of Ni-25.3 at.% Si alloys to high cooling rates using the drop-tube technique, wherein $Ni_{25}Si_9$ formed as the dominant phase for all particle sizes, with γ-$Ni_{31}Si_{12}$ and β_1-Ni_3Si also being present. Moreover, they revealed an hitherto unobserved β_1 - $Ni_{25}Si_9$ eutectic, which formed as both a regular lamellar and an anomalous eutectic, depending upon the cooling rate and undercooling experienced by the droplet. At high cooling rates, the lamellar structure consisted of very fine alternating lamellar of $Ni_{25}Si_9$ (≈ 200 nm) and β_1-Ni_3Si (≈ 20 nm), with the fine lamellar spacing being attributed to a very low diffusivity in the melt. This was in turn attributed to the existence of a covalently bonded Si-Si network. Moreover, they found that at the highest cooling rates an increasing fraction of droplets solidified to near single phase $Ni_{25}Si_9$. Given this formation of single phase $Ni_{25}Si_9$, Cao et al. also took the opportunity to study the thermodynamic properties of the $Ni_{25}Si_9$ phase by in-situ heating during XRD analysis and by DTA. This showed the decomposition of $Ni_{25}Si_9$ to β_1 and γ-$Ni_{31}Si_{12}$ for temperatures in excess of 790 K.

The formation of $Ni_{25}Si_9$ has not been observed during undercooling experiments on Ni-21.4 at.% alloys [16, 17], with only a small fraction being observed in Ni-25.3 at.% Si alloy [19]. Conversely, when high cooling rates are applied, it is readily obtained in alloys of eutectic composition. Leonhardt et al. [21] have demonstrated this by quenching the undercooled

eutectic onto a chilled substrate, while Dutra et al. [25] found similar results using the melt-spinning technique. By analogy with these earlier studies, Cao et al. attributed the formation and retention of the metastable $Ni_{25}Si_9$ phase to the high cooling rates experienced during drop-tube solidification processing. However, the initial composition of the melt, close to the stoichiometry of the $Ni_{25}Si_9$ phase, would also favour its formation if long range diffusion in the melt were suppressed by a low atomic mobility resulting from the high viscosity of the melt.

In the present work, the rapid solidification of $Ni_{64.7}Fe_{10}Si_{25.3}$ and $Ni_{59.7}Fe_{15}Si_{25.3}$ alloys was studied in a 6.5 m drop-tube to investigate the phase formation and microstructural development in Ni-Fe-Si alloys at high cooling rates. Chemically, Ni and Fe are very similar, so direct substitution of Fe for Ni might be expected for samples doped with low concentrations of Fe. Fig. 1b is the Ni-rich corner of the Ni-Fe-Si ternary phase diagram at 1400 K, calculated using the CALPHAD software package MTDATA [26], with version 5.0 of the SGTE Solutions Database SGSOL. It is clear that both the $Ni_{64.7}Fe_{10}Si_{25.3}$ and $Ni_{59.7}Fe_{15}Si_{25.3}$ alloys are on the hypereutectic side of the α-γ eutectic, the β-Ni_3Si phase being suppressed by the presence of iron. This is also illustrated in Fig. 1c, which shows a pseudobinary isopleth diagram in which the end members are the Ni_3Si and Fe_3Si compositions, also calculated, as above, using the MTDATA software. Complete suppression of the formation of β can be observed for Fe concentrations in excess of 6.5 at.%. Therefore, the predicted solidification path would be for single phase γ to form first, which will lower the Si concentration of the remaining liquid until this equals the eutectic composition, wherein the residual liquid will solidify to the α-γ eutectic structure.

2 Experimental

Master alloys of the required composition were prepared by arc-melting the elemental constituents (purity = 99.99% Ni, 99.999% Si and 99.9% Fe) under a protective argon atmosphere. The arc-melting process was repeated 5 times to ensure uniform mixing of the final sample.

Approximately 15 g of the alloy was loaded into an alumina crucible with 3 laser drilled holes (300 μm diameter) in the base. The crucible was placed in an RF coil fixed at the top of the 6.5 m drop-tube. The drop-tube was evacuated to a pressure of 4×10^{-3} Pa and back-filled with dried, oxygen free N_2 gas to a pressure of 50 kPa, this procedure being repeated three

times prior to melting to ensure the tube was thoroughly flushed. Melting of the alloy was by induction of heating of a graphite susceptor enclosing the alumina crucible, with temperature determination by means of an R-type thermocouple inside the crucible. When the desired superheat was achieved the melt was ejected by pressurising the crucible with 0.4 MPa of N_2 gas. Spherical droplets, with diameters in the range of 53-850 μm, were collected at the bottom of the drop-tube and classified into standard size ranges by sieving. The sizes of the sieves used here were 850 μm, 500 μm, 300 μm, 212 μm, 150 μm, 106 μm, 75 μm and 53 μm.

Particles of each size range were hot mounted using Transoptic resin. The mounted samples were ground flat using a series of progressively finer SiC papers, starting with 240, 400, 800 and lastly 1200 grit, with optical microscopy being used to check the quality of the surface finish at each stage. Once the samples were appropriately ground they were polished using 6 μm, 3 μm, 1 μm and 0.25 μm diamond paste. The samples were washed using dilute detergent and methanol and then dried using hot air between each polishing step.

Phase identification was undertaken on mounted and polished samples by X-ray diffraction using a Philips PANalytical Diffractometer with Cu K_α radiation. However, particularly for the largest particles, we are unable to guarantee that the mounted particles do not have any preferred orientation, and for this reason the analysis is considered as qualitative only, that is we have identified the phases present but have not attempted to undertake Rietveld refinement in order to estimate the volume fractions of those phases. Instead, in the present work, the phase formation and overall structural evolution were studied by the combination of XRD, SEM and TEM analysis. The composition of the polished samples was characterized using EDX detection mounted on a LEO 1530 Gemini FEGSEM and by microprobe analysis (Jeol 8230). Once composition analysis was complete the polished samples were etched using a mixture of Hydrofluoric Acid (5ml), Hydrogen Peroxide (5ml) and water (30ml) to reveal the microstructure for further SEM analysis. FIB was used to prepare TEM specimens, which were subsequently analysed using an FEI Tecnai F20 FEG-TEM.

3 Results

3.1 XRD Analysis

Fig. 2 shows the XRD patterns for the $Ni_{64.7}Fe_{10}Si_{25.3}$ alloy as a function of particle size. It can be seen that the γ-$Ni_{31}Si_{12}$ phase is observed in the XRD patterns for all particle sizes. For the smallest droplets (75-106 μm and 53-75 μm), additional peaks are observed, which can be

indexed to the reflections of the metastable phase $Ni_{25}Si_9$. A similar result is also observed in the $Ni_{59.7}Fe_{15}Si_{25.3}$ alloy, the XRD patterns for which shown in Fig. 3. Again, the presence of γ-$Ni_{31}Si_{12}$ is observed in all size fractions, while the presence of $Ni_{25}Si_9$ is noted only in relatively small particles (53-150 μm). However, the relative peak intensities for $Ni_{25}Si_9$ in the 53-106 μm size fraction of the $Ni_{59.7}Fe_{15}Si_{25.3}$ alloy are much stronger than that for the $Ni_{64.7}Fe_{10}Si_{25.3}$ alloy, which might imply a higher fraction of the $Ni_{25}Si_9$ phase in the $Ni_{59.7}Fe_{15}Si_{25.3}$ alloy. This will be explored further using SEM and TEM analysis. There is one common problem in the XRD analysis of both alloys, namely that it is difficult to distinguish the α-Ni and β_1-Ni_3Si phases, both phases having the same cubic structure, with the lattice constants being a = 3.5244 Å and 3.5050 Å, respectively. Therefore, differentiation of these two phases has been undertaken using TEM. We note that if it is the α phase being observed the result would be consistent with the equilibrium phase diagram.

3.2 Microstructure and Phase Identification

Microstructural analysis reveals that, irrespective of the alloy system, all droplets can be classified as containing one or more of three typical microstructures. As shown in Fig. 4, these comprise: (I) a regular structure consisting of a single phase and a eutectic structure; (II) a refined lamellar structure; (III) an anomalous structure with a fine phase dispersed in a single phase matrix. To confirm the origin of these three different structures, FIB was used to prepare two TEM specimens, as shown in Fig. 5, one for the regular structure and the other for the fine lamellar and anomalous structures, in a droplet in which these two structures were found to co-exist. TEM selected area diffraction patterns confirm that the bulk phase (I_1) and one of the eutectic phases (I_2) found in structure I is γ-$Ni_{31}Si_{12}$ (Fig. 6). A selected area diffraction pattern from I_3, the other component of the eutectic structure present in morphology I, displays super-lattice spots (Fig. 6b). This indicates that I_3 is the ordered $L1_2$ phase and not the α phase expected from the equilibrium phase diagram. Here, by analogy with the Ni-Si binary system, we label it as the β_1 phase. A further selected area diffraction pattern analysis confirms that the wide band (I_4) in the fine lamellar structure (morphology II) is also γ-$Ni_{31}Si_{12}$ (Fig. 7a), while the matrix-phase (I_5) in the anomalous structure (morphology III) is identified as the metastable phase, $Ni_{25}Si_9$, as shown in Fig. 7b.

For both the $Ni_{64.7}Fe_{10}Si_{25.3}$ and $Ni_{59.7}Fe_{15}Si_{25.3}$ alloys, all of the large droplets (212-850 μm) comprise only the regular structure, I. In the smaller droplets (< 212 μm), some samples also comprise only the regular structure, while the remainder of the droplets present either a

mixed structure comprising morphology I together with morphologies II and/or III (Fig. 8 – Fig. 10) or comprise only the anomalous structure, III (Fig. 11). In order to understand the microstructural evolution with increasing cooling rate, the droplets were classified into three different categories (A, B and C) according to microstructural characteristics which were easy to distinguish under optical microscopy and for large number of particles. Type A droplets are defined as comprising only the regular structure (I). Type B droplets present mixed structures, comprising morphology I, together with one, or both, of morphologies II and III. Type C droplets comprise only the anomalous structure, III. However, because it is difficult to distinguish mixed structures comprising morphologies II and III (Fig. 10) under optical microscopy, these droplets were also classified as type C. This information is summarised in Table I.

The fractions of these three types of particles have been counted. The numbers of particles counted for the $Ni_{64.7}Fe_{10}Si_{25.3}$ alloy were 463 (150-212 μm), 514 (106-150 μm), 2182 (75-106 μm) and 1844 (53-75 μm), while the numbers for the $Ni_{59.7}Fe_{15}Si_{25.3}$ alloy were 219 (150-212 μm), 505 (106-150 μm), 692 (75-106 μm) and 1909 (53-75 μm). The count results are shown in Fig. 12a.

For the $Ni_{64.7}Fe_{10}Si_{25.3}$ alloy, the fraction of type A particles is 100% in the large size ranges (212-850 μm), decreasing slightly to 98.5 % for the intermediate size fraction (150-212 μm) and then dropping rapidly to 28.69% for the smallest size range (53-75 μm). Correspondingly, the fraction of type B droplet increases from 1.5% (150-212 μm) to 31.21% (53-75 μm) for these intermediate to small diameter droplets. Type C particles are first observed in the 106-150 μm size range, with the fraction present being 8.56 %. This increases to 39.1% for the 53-75 μm diameter particles. For the $Ni_{59.7}Fe_{15}Si_{25.3}$ alloy, the fraction of type A droplet follows a similar trend, namely that 100% of the coarsest particles (212-850 μm) display only morphology I reducing to 14.82% for the finest particles (53-75 μm). The total fraction of type B and C particles increases as the diameter decreases, this being 66.62% in the 75-106 μm size range and reaching to 85.17% for the smallest particles (53-75 μm). In contrast to the results found for the $Ni_{64.7}Fe_{10}Si_{25.3}$ alloy, the fraction of type C particle increases monotonically from 29.11% (150-212 μm) to 82.24% (53-75 μm), while the proportion of the type B particle decreases to 2.93% (53-75 μm) after reaching a maximum of 18.02% (106-150 μm).

From the above analysis it is clear that the metastable phase $Ni_{25}Si_9$ is restricted to the anomalous structure III. This is a constituent of the type B and type C droplets, it being the dominant morphology in this latter droplet type. Therefore, the count result, displaying an increasing fraction of type B and C droplets with decreasing particle size, irrespective of the alloy composition, is consistent with the strong intensity of the $Ni_{25}Si_9$ peaks in the XRD patterns for the small droplets. Conversely, peaks for $Ni_{25}Si_9$ are not observed in the XRD patterns of droplets in the 106-850 μm size range for $Ni_{64.7}Fe_{10}Si_{25.}3$ alloy and in the 150-850 μm size range for $Ni_{59.7}Fe_{15}Si_{25.3}$ alloy. We note from Figure 12a that there is microstructural evidence for the presence of low levels of $Ni_{25}Si_9$ (identification of Type C droplets) in some of the larger size fractions (e.g. 150-212 μm) when the presence of this phase is not apparent in the XRD patterns from these size ranges. Indeed, from Fig. 12a we would judge that the sample needs to contain > 30% $Ni_{25}Si_9$ by volume before a clear XRD signature is discernable. This is probably related to the two characteristic peaks at 46.4° and 46.9° corresponding to high order reflections (<1 1 $\bar{4}$> and <3 0 0> respectively). We also note the higher prevalence of type C droplets in the $Ni_{59.7}Fe_{15}Si_{25.3}$ alloy, which is consistent with the stronger $Ni_{25}Si_9$ diffraction peaks for this composition.

On the basis that the Type C droplets are almost exclusively $Ni_{25}Si_9$ (taken as (96 ± 2)%) and from a visual estimate that on average the Type B droplets contain (10 ± 5)% $Ni_{25}Si_9$, we have estimated in Fig. 12b the variation in the $Ni_{25}Si_9$ content of the droplets as a function of diameter and composition. The error bars reflect our uncertainty in assigning the volume fraction of $Ni_{25}Si_9$ to the particular droplet morphology (Type B or C) and where no error bar is shown this is because it would be smaller than the plotting symbol used.

The microstructures of the 150-212 μm diameter droplets for the $Ni_{64.7}Fe_{10}Si_{25.3}$ alloy have been studied in detail, since the change from morphology I to morphologies II and III is first observed in this size range for both alloys. With 463 particles being mounted and analyzed, 456 particles present only the regular structure, I, (type A) with only 5 particles presented a mixed structure of regular, I, and refined lamellar, II, morphology (type B). The remaining 2 particles included all three typical morphology. Fig. 13 shows the direct transition from the coarse lamellar structure to fine lamellar structure. In addition, Fig. 14 and the insets (1 and 3) in Fig. 8 indicate that the fine lamellar structure can also develop from the normal surface of single phase γ-$Ni_{31}Si_{12}$ or $Ni_{25}Si_9$.

The fine lamellar structure (II) is only rarely found in particles of the $Ni_{59.7}Fe_{15}Si_{25.3}$ alloy, wherein the type B droplets mainly consist of the morphologies I and III. Moreover, the 150-212 μm diameter particles of the $Ni_{59.7}Fe_{15}Si_{25.3}$ alloy show a slightly different microstructural evolution, with a tendency for a transition direct from morphology I to morphology III and with less prevalence of morphology II, the refined lamellar structure.

3.3 EDX Analysis

The average elemental compositions of the bulk droplets, together with the local composition of the γ-$Ni_{31}Si_{12}$ phase were measured using EDX. In each size range, area scans on at least 10 random particles were performed to determine the bulk average composition. To determine the composition of γ-$Ni_{31}Si_{12}$, 20 spectra were obtained from different grains. Fig. 15a shows the results for the $Ni_{64.7}Fe_{10}Si_{25.3}$ alloy, indicating that the average composition of droplets in all size fractions are similar, with the average composition being 10.57 at.%, 25.07 at.% and 64.36 at.% for Fe, Si and Ni respectively. These are consistent with the nominal composition of the alloy to within the expected experimental uncertainty associated with EDX determination. The compositions of the γ-$Ni_{31}Si_{12}$ phase in all size fractions of the type A droplets are also very similar, with the average values being 6.99 at.%, 27.15 at.% and 65.86 at.% for Fe, Si and Ni respectively. We note that the Si composition is higher than that of the melt but close to the stoichiometry of the γ-$Ni_{31}Si_{12}$ phase and that the Fe composition is lower than that of the melt. A similar result is observed for the $Ni_{59.7}Fe_{15}Si_{25.3}$ alloy, as shown in Fig. 15b. The average composition of the droplets is 15.65 at.%, 24.83 at.% and 59.52 at.% for Fe, Si and Ni, again very close to the nominal composition of the melt. The Fe composition of the γ-$Ni_{31}Si_{12}$ phase is 11.32 at.%, which is again lower than that of the melt. However, the Si composition of the γ-$Ni_{31}Si_{12}$ phase is 27.01 at.%, which is higher than that of the melt and close to the stoichiometry of the γ-$Ni_{31}Si_{12}$ phase. These results are consistent the substitution of Fe for Ni in the γ-phase.

For the droplets of the $Ni_{64.7}Fe_{10}Si_{25.3}$ alloy the composition of the eutectic area in the regular structure was checked by Microprobe analysis, with 15 different areas being analysed. The Si composition was determined as 20.63 at.%. The Fe composition is 19.11 at.%, indicating that surplus Fe accumulates in the eutectic areas. A similar result is observed in $Ni_{59.7}Fe_{15}Si_{25.3}$ alloy, as shown in Fig. 16a.

The average composition of the type C particles (morphology III) was measured to be 10.54 at.%, 25.04 at.% and 64.42 at.% (for Fe, Si and Ni) in the $Ni_{64.7}Fe_{10}Si_{25.3}$ alloy, and 15.58

at.%, 24.95 at.% and 59.47 at.% in the $Ni_{59.7}Fe_{15}Si_{25.3}$ alloy respectively. This indicates that the composition of the anomalous structure is close to the composition of the respective bulk alloy. This is consistent with the identification that the matrix of the anomalous structure is single-phase $Ni_{25}Si_9$ (with Fe substituting for Ni). Line scan results for adjacent regions of the anomalous and regular structures (Fig. 16b), show that the average Ni, Fe and Si composition of the metastable phase is in between the average values of the gamma phase and the eutectic area.

4 Discussion

According to the XRD diffraction patterns, only the γ-$Ni_{31}Si_{12}$ and β_1 phases are formed in the larger droplets, while the additional phase $Ni_{25}Si_9$ is formed in the smaller droplets. This is in contrast to the results for drop-tube solidified Ni-25.3 at.% Si alloy, wherein $Ni_{25}Si_9$ formed as the dominant phase in all size ranges. The formation of the metastable phase $Ni_{25}Si_9$ in Ni-Fe-Si alloys has not previously been reported and indicates that there is an extended $Ni_{25}Si_9$ stability field in the Ni-rich part of the Ni-Fe-Si phase diagram at high undercoolings, and/or high cooling rates. Unfortunately, due to the lack of thermodynamic data relating to the $Ni_{25}Si_9$ phase, it is not possible to perform any form of CALPHAD type calculation to elucidate the influence of Fe on the stability of $Ni_{25}Si_9$. However, the results presented here, particularly those in Figures 12a and b, would suggest, perhaps somewhat paradoxically, that low Fe concentrations are rather more effective at suppressing the formation of $Ni_{25}Si_9$ than are higher concentrations.

As can be seen in Fig. 4, the regular structure (I) seems superficially to be as expected from the equilibrium phase diagram, i.e. for a hyper-eutectic composition we observe single phase regions and a eutectic. TEM analysis confirms that the single phase regions (I_1) and one of the phases (I_2) in the eutectic are γ. According to the equilibrium phase diagram, the other phase, I_3, in the eutectic should be α-Ni. However, the TEM diffraction pattern from the phase I_3 displays super-lattice reflections, which identifies I_3 as the $L1_2$ (β_1) phase and not α-Ni. Unfortunately, the individual phases within the eutectic structure are too fine to make reliable composition measurements. However, the bulk average composition of the eutectic structure in the droplets of the $Ni_{64.7}Fe_{10}Si_{25.3}$ alloy can be determined and is 60.27, 19.11 and 20.63 at.% for Ni, Fe and Si respectively. On the assumption that the composition of the γ phase in the eutectic is the same as that of the single phase γ region, and knowing the bulk composition of the eutectic region, we can estimate the approximate composition of the $L1_2$

phase. High resolution TEM images allow us to estimate the volume ratio of the phases $L1_2$:γ as 1.2±0.2, wherein we would estimate the composition of the $L1_2$ region via a mass balance calculation to be 25.75±1.34 at.%, 17.18±0.69 at.% and 57.07±0.65 at.% for Fe, Si and Ni respectively. With reference to the ternary phase diagram, an alloy with this composition would be within the α-Ni stability field. However, the eutectic formed here is between γ and β_1, which suggests that under rapid cooling Fe stabilises the formation of the $L1_2$ (β_1) phase. Moreover, noting the Si content is ≈ 17 at.%, we would surmise that there must be some substitution of Fe for Si in the $L1_2$ phase.

The formation of the $L1_2$ phase in Ni-rich Ni-Fe-Si alloys has previously been studied by Himuro et al. [27, 28], who observed that the $L1_2$ phase precipitated from the α matrix by aging of a $Ni_{60}Fe_{30}Si_{10}$ alloy for short periods. They also studied the solidification behaviour of $Ni_{75}Fe_{15}Si_{10}$ and $Ni_{75}Fe_{13}Si_{12}$ alloys wherein, clear evidence for the substitution of Fe for Si, rather than Ni, was found. Himuro et al. suggested that in the Ni-Fe-Si system, Fe atoms occupy different substitutional sites depending upon the alloy composition, i.e. Fe atoms occupy the Si sites in the composition region around 75 at.% Ni, but substitute for Ni atoms otherwise. They, therefore, attributed the formation of the $L1_2$ ordered phase to the fact that Fe atoms have a tendency to mainly substitute for Si in the Ni_3Si phase, and consequently, the $L1_2$ phase was represented by Ni_3(Si, Fe) in their work. This is consistent with our observation that the $L1_2$ phase formed instead of α-Ni at the relatively low Si composition of 17.18 at.%. This would imply that in the $Ni_{64.7}Fe_{10}Si_{25.3}$ alloy studied here, the $L1_2$ phase formed with approximately 1 in 3 of the Si sites occupied by Fe atoms. We note however, that there is no evidence for the substitution of Fe for Si in the γ-$Ni_{31}Si_{12}$ phase, the measured Si compositions being 27.15 at.% and 27.01 at.% for the $Ni_{64.7}Fe_{10}Si_{25.3}$ and $Ni_{59.7}Fe_{15}Si_{25.3}$ alloys respectively, both of which are close to the stoichiometry of γ-$Ni_{31}Si_{12}$ (27.91 at.%). Instead, these results appear to indicate the substitution of Fe for Ni, and not Si, in γ which is consistent with the chemical similarity of Fe and Ni. TEM analysis confirms that the $L1_2$ phase obtained in the present work is single phase (Fig. 17), i.e. we are not seeing a mixture of the α and $L1_2$ phases, which would skew the estimated composition analysis for the $L1_2$ phase. Therefore, these results are consistent with the description by Himuro et al. that the Fe atoms present different behaviour substitution behaviour depending upon the Ni concentration of the host phase.

In terms of the droplet morphologies observed, as opposed to the phases present, a fairly straightforward picture may be put forward. The largest droplets will experience both low cooling rates and, therefore, relatively low undercooling. Near equilibrium solidification is experienced which, for a hypereutectic alloy, will result in the growth of single phase γ followed by solidification of the eutectic. These are the droplets we have categorised as Type A. The caveat however is that, as discussed above, the eutectic formed is between γ and β, rather than between γ and α, as would be expected from the equilibrium diagram. Conversely, the smallest droplets will experience the highest cooling rates and, therefore on average, also high undercooling, wherein the melt may be undercooled directly into the $Ni_{25}Si_9$ stability field. Given the proximity of the $Ni_{25}Si_9$ stoichiometry (26.47 at.% Si) to the composition of the melt, solidification to (near) single phase $Ni_{25}Si_9$ results. These are the droplets we have categorised as Type C.

The most complex microstructural evolution is observed in droplets in the intermediate size range, wherein a range of mixed structures arises (Type B droplets). Here, we attribute this variation to the interplay of cooling rate and undercooling. To a good first approximation, droplets of the same size will be subjected to the same cooling rate. However, it is not true that all droplets of the same size will solidify at the same undercooling, as this is controlled by nucleation which is a stochastic process. Solidification of the liquid might be catalysed by a potent nucleation site, such as an oxide, and in such cases, deep undercooling would not be expected. However, the catalytic effect of active nuclei can be restricted by dispersing the liquid into a large number of small droplets that solidify individually [29], as is the case in the drop-tube. In this stochastic process, a range of undercoolings will result. At a given particle diameter an upper limit to the undercooling achieved can be estimated from the average nuclei density in the melt according to the model of [20], but many droplets will achieve a much lower undercooling. Estimates of the cooling rate and undercooling in the drop-tube environment are given in Fig. 18, with the parameters used in this calculation being given in Appendix 1. Within the intermediate size ranges droplets may experience both high (Type C) and low (Type A) undercooling as well as those displaying mixed morphologies (Type B).

Where mixed structures are observed within a single droplet this could be due to multiple nucleation. In the model described by Ahamd et al. [19], it has been postulated that the viscosity of the melt with 25 at. % Si is high due to the existence of a covalently bonded Si-Si network. Under the conditions of a rapidly cooling droplet and a sluggish growth front, multiple nucleation might be favoured if the liquid ahead of the growth front cools

significantly prior to the growth front reaching it, thereby activating more nuclei in the melt. In this model the mixed structures I and III would result from independent, but near simultaneous, multiple nucleation events. Furthermore, the refined lamellar structure might result from the solidification of the remaining liquid, resulting in the mixed structure of types I, II and III. There are also some droplets containing a small fraction of the refined lamellar structures, which are surrounded by a large fraction of the anomalous structure, as shown in Fig. 10. This might imply that, in the final stage of the anomalous structure formation, the solidification converted to the growth of the refined lamellar structure.

5 Conclusions

$Ni_{64.7}Fe_{10}Si_{25.3}$ and $Ni_{59.7}Fe_{15}Si_{25.3}$ alloys have been rapidly solidified from their parent melts by drop-tube processing, wherein the following conclusions can be derived from the present work.

1) In both the $Ni_{64.7}Fe_{10}Si_{25.3}$ and $Ni_{59.7}Fe_{15}Si_{25.3}$ alloys, the metastable phase $Ni_{25}Si_9$ was obtained for droplets < 212 μm in diameter, with the corresponding critical cooling rate being 5.1×10^3 K s^{-1}. This indicates that there is an extended stability field for $Ni_{25}Si_9$ in the Ni-rich part of the Ni-Fe-Si ternary phase diagram.
2) Three typical microstructures were observed with decreasing particle size (and therefore increasing cooling rate). (I) a regular structure consisting of single phase γ and a eutectic between the γ and β_1-Ni_3Si phases; (II) a refined lamellar structure with wide (50 nm) bands of γ-$Ni_{31}Si_{12}$ and narrow (< 10 nm) bands of β_1-Ni_3Si (III) an anomalous structures consisting of a matrix of the metastable phase $Ni_{25}Si_9$ with small inclusions of another, as yet unidentified, phase.
3) With decreasing droplet size an increasing fraction of droplets experience high undercoolings and therefore can be undercooled into the $Ni_{25}Si_9$ stability field, forming the anomalous structure.
4) The Si compositions of the single phase γ-$Ni_{31}Si_{12}$ regions in the $Ni_{64.7}Fe_{10}Si_{25.3}$ and $Ni_{59.7}Fe_{15}Si_{25.3}$ alloys are the same, being 27.15 at.% and 27.01 at.%, and are close to the stoichiometry of the γ phase, while the corresponding Fe compositions are different, being 6.99 at.% and 11.32 at.%. This appears to indicate the substitution of Fe for Ni, and not Si, in the γ-phase. Conversely, Fe appears to stabilise the $L1_2$ phase as a γ-β eutectic is observed rather than a α-γ eutectic predicted by ternary phase diagram, wherein the substitution of Fe for Si occurs in the $L1_2$ phase.

Acknowledgements

The authors acknowledge financial supports of the China Scholarship Council (CSC) – University of Leeds scholarship program.

Appendix 1

The physical parameters of the gas and alloy used to calculate the cooling rate and undercooling are given in Table 2.

6 Reference

[1] Miura S, Ohkubo K, Mohri T. Mechanical properties of Co-based $L1_2$ intermetallic compound $Co_3(Al,W)$. Mater trans 2007; 48: 2403-8. DOI:10.2320/matertrans.MAW200734

[2] Fleischer RL. High-strength, high-temperature intermetallic compounds. J Mater Sci 1987; 22: 2281-8. DOI:10.1007/BF01082105

[3] Schulson EM, Briggs LJ, Baker I. The strength and ductility of Ni_3Si. Acta Metall Mater 1990; 38: 207-13. DOI:10.1016/0956-7151(90)90050-Q

[4] Stoloff NS, Liu CT, Deevi SC. Emerging applications of intermetallics. Intermetallics 2000; 8: 1313-20. DOI:10.1016/S0966-9795(00)00077-7

[5] Takasugi T, Suenaga H, Izumi O. Environmental effect on mechanical properties of recrystallized $L1_2$-type $Ni_3(Si,Ti)$ intermetallics. J Mater Sci 1991; 26: 1179-86. DOI:10.1007/BF00544452

[6] Ward-Close CM, Minor R, Doorbar PJ. Intermetallic-matrix composites-a review. Intermetallics 1996; 4: 217-29. DOI:10.1016/0966-9795(95)00037-2

[7] Yang JM. The mechanical behavior of *in-situ* NiAl-refractory metal composites. JOM 1997; 49: 40-3. DOI:10.1007/BF02914401

[8] Milenkovic S, Caram R. Effect of the growth parameters on the Ni–Ni_3Si eutectic microstructure. J Cryst Growth 2002; 237-239: 95-100. DOI:10.1016/S0022-0248(01)01875-9

[9] Herlach DM. Non-equilibrium solidification of undercooled metallic melts. Mater Sci Eng R Rep 1994; 12: 177-272. DOI:10.1016/0927-796X(94)90011-6

[10] Kaneno Y, Wada M, Inoue H, Takasugi T. Effects of Grain Size and Temperature on Environmental Embrittlement of $Ni_3(Si, Ti)$ Alloy. Mater Trans 2001; 42: 418-21.

[11] Schulson EM, Barker DR. A brittle to ductile transition in NiAl of a critical grain size. Scr Metall 1983; 17: 519-22. DOI:10.1016/0036-9748(83)90344-7

[12] Cahn RW, Siemers PA, Geiger JE, Bardhan P. The order-disorder transformation in Ni_3Al and Ni_3Al· Fe alloys-I. Determination of the transition temperatures and their relation to ductility. Acta Metall 1987; 35: 2737-51. DOI:10.1016/0001-6160(87)90273-2

[13] Cahn RW, Siemers PA, Hall EL. The order-disorder transformation in Ni_3Al and Ni_3Al· Fe alloys-II. Phase transformations and microstructures. Acta Metall 1987; 35: 2753-64. DOI:10.1016/0001-6160(87)90274-4

[14] Liu F, Chen Y, Yang G, Lu Y, Chen Z, Zhou Y. Competitions incorporated in rapid solidification of the bulk undercooled eutectic $Ni_{78.6}Si_{21.4}$ alloy. J Mater Res 2007; 22: 2953-63. DOI:10.1557/JMR.2007.0380

[15] Lu Y, Liu N, Shi T, Luo D, Xu W, Li T. Microstructure and hardness of undercooled $Ni_{78.6}Si_{21.4}$ eutectic alloy. J Alloy Compd 2010; 490: L1-L4. DOI:10.1016/j.jallcom.2009.09.038

[16] Lu Y, Liu F, Yang G, Wang H, Zhou Y. Grain refinement in solidification of highly undercooled eutectic Ni–Si alloy. Mater Lett 2007; 61: 987-90. DOI:10.1016/j.matlet.2006.06.028

[17] Goetzinger R, Barth M, Herlach DM. Mechanism of formation of the anomalous eutectic structure in rapidly solidified Ni–Si, Co–Sb and Ni–Al–Ti alloys. Acta Mater 1998; 46: 1647-55. DOI:10.1016/S1359-6454(97)00339-X

[18] Çadırlı E, Herlach DM, Volkmann T. Characterization of rapidly solidified Ni-Si and Co-Al eutectic alloys in drop tube. J Non-Cryst Solids 2010; 356: 461-6. DOI:10.1016/j.jnoncrysol.2009.12.019

[19] Ahmad R, Cochrane RF, Mullis AM. The formation of regular αNi-γ($Ni_{31}Si_{12}$) eutectic structures from undercooled Ni–25 at.% Si melts. Intermetallics 2012; 22: 55-61. DOI:10.1016/j.intermet.2011.10.021

[20] Cochrane RF, Greer AL, Eckler K, Herlach DM. Dendrite growth velocities in undercooled Ni· Si alloys. Mater Sci Eng A 1991; 133: 698-701. DOI:10.1016/0921-5093(91)90165-J

[21] Leonhardt M, Löser W, Lindenkreuz HG. Metastable phase formation in undercooled eutectic $Ni_{78.6}Si_{21.4}$ melts. Mater Sci Eng A 1999; 271: 31-7. DOI:10.1016/S0921-5093(99)00161-6

[22] Cao L, Cochrane RF, Mullis AM. Lamella structure formation in drop-tube processed Ni–25.3 at.% Si alloy. J Alloy Compd; In Press. DOI:10.1016/j.jallcom.2013.11.233

[23] Mullis AM, Cao L, Cochrane RF. Non-equilibrium processing of Ni-Si alloys at high undercooling and high cooling rates. Mater Sci Forum 2014; 790-791: 22-7. DOI:10.4028/www.scientific.net/MSF.790-791.22

[24] Cao L, Cochrane RF, Mullis AM. Microstructural evolution and phase formation in rapidly solidified Ni-25.3 at.% Si alloy. Unpublished results.

[25] Dutra AT, Milenkovic S, Kiminami CS, Santino AM, Gonçalves MC, Caram R. Microstructure and metastable phase formation in a rapidly solidified Ni-Si eutectic alloy using a melt-spinning technique. J Alloy Compd 2004; 381: 72-6. DOI:10.1016/j.jallcom.2004.02.059

[26] MTDATA is a CALPHAD (Calculation of Phase Diagrams) package licensed by the National Physical Laboratory, UK. Functionality is similar to other CALPHAD packages such as thermoCalc.

[27] Himuro Y, Tanaka Y, Kamiya N, Ohnuma I, Kainuma R, Ishida K. Stability of ordered $L1_2$ phase in Ni_3Fe–Ni_3X (X: Si and Al) pseudobinary alloys. Intermetallics 2004; 12: 635-43. DOI:10.1016/j.intermet.2004.03.008

[28] Himuro Y, Tanaka Y, Ohnuma I, Kainuma R, Ishida K. Phase equilibria and γ'-$L1_2$ phase stability in the Ni-rich portion of Ni-Fe-Si and Ni-Fe-Al systems. Intermetallics 2005; 13: 620-30. DOI:10.1016/j.intermet.2004.10.009

[29] Herlach DM, Cochrane RF, Egry I, Fecht HJ, Greer AL. Containerless processing in the study of metallic melts and their solidification. Int Mater Rev 1993; 38: 273-347. DOI: 10.1179/095066093790326267

[30] Libera M, Olson GB, Vander S. Heterogeneous nucleation of solidification in atomized liquid metal droplets. Mater Sci Eng A 1991; 132: 107-118.

[31] Coker AK. Ludwig's applied process design for chemical and petrochemical plants. 4th ed. Burlington: Gulf Professional Publishing; 2007.

[32] Cole WA, Wakeham WA. The viscosity of nitrogen, oxygen, and their binary mixtures in the limit of zero density. J Phys Chem Ref Data 1985; 14: 209-26. DOI: 10.1063/1.555748
[33] Latto B, Saunders MW. Viscosity of nitrogen gas at low temperatures up to high pressures: a new appraisal. Can J Chem Eng 1972; 50: 765-70. DOI:10.1002/cjce.5450500615
[34] Smith JM, Van Ness HC, Abbott MM. Introduction to Chemical Engineering Thermodynamics. 4th ed. New York: McGraw-Hill Publishing Company; 1975.
[35] Gillessen F, Herlach DM. Crystal nucleation and glass-forming ability of Cu • Zr in a containerless state. Mater Sci Eng 1988; 97: 147-51. DOI: 10.1016/0025-5416(88)90030-4
[36] Gale WF, Totemeier TC. Smithells metals reference book, 8th ed. Oxford: Butterworth-Heinemann; 2004.

Figures and Tables Caption

Fig. 1. (a) Ni-rich part of the Ni-Si phase diagram; (b) Ni-rich corner of the Ni-Fe-Si equilibrium ternary phase diagram at 1400 K. The points labelled 1 and 2 represent the notional composition of the $Ni_{64.7}Fe_{10}Si_{25.3}$ and $Ni_{59.7}Fe_{15}Si_{25.3}$ alloys; (c) Vertical section diagram of the Ni_3Si-Fe_3Si pseudo-binary system.

Fig. 2. XRD results from the $Ni_{64.7}Fe_{10}Si_{25.3}$ alloy as a function of size range, showing evidence for the presence of the additional phase $Ni_{25}Si_9$, in droplets in the 53-106 μm size ranges. Note that for clarity only the interval 40°-50° is shown.

Fig. 3. XRD results from the $Ni_{59.7}Fe_{15}Si_{25.3}$ alloy as a function of size range, showing evidence for the presence of the additional phase $Ni_{25}Si_9$, in droplets in the 53-106 μm size ranges. Note that for clarity only the interval 40°-50° is shown.

Fig. 4. Micrographs of the three characteristic microstructures observed in the $Ni_{64.7}Fe_{10}Si_{25.3}$ and $Ni_{59.7}Fe_{15}Si_{25.3}$ drop-tube samples: (a) regular microstructure, I, from 212-300 μm droplet of $Ni_{64.7}Fe_{10}Si_{25.3}$ alloy; (b) refined lamellar structure, II, from 150-212 μm droplet of $Ni_{64.7}Fe_{10}Si_{25.3}$ alloy; (c) anomalous structure, III, from 150-212 μm droplet of $Ni_{59.7}Fe_{15}Si_{25.3}$ alloy. (d) TEM bright field image showing the refined lamellar structure in (b).

Fig. 5. Micrographs showing the regions from which TEM specimens were taken (white rectangles). (a) and (b) are taken from the 300-500μm and 53-75 μm sieve fraction respectively of the $Ni_{64.7}Fe_{10}Si_{25.3}$ alloy. The black rectangles, T_1, T_2 and T_3, refer to the areas analysed by TEM, to confirm the identity of the phases, I_1-I_5.

Fig. 6. (a) The results of the TEM analysis on the area, T_1, identifying that the single phase (I_1) is γ-$Ni_{31}Si_{12}$, and that the eutectic structure consists of γ-$Ni_{31}Si_{12}$ (I_2) and the ordered $L1_2$ phase (I_3); (b) TEM selected area diffraction pattern of the area shown circled in (a), displaying the super-lattice reflections from the $L1_2$ ordered structure.

Fig. 7. TEM micrographs of the refined lamellar (II) and anomalous (III) structures, with, inset, diffraction patterns identifying (a) T_2, wide band I_4, as γ-$Ni_{31}Si_{12}$; (b) T_3, primary coarse phase I_5, as the metastable phase $Ni_{25}Si_9$.

Fig. 8. SEM images showing the microstructure of one 150-212 μm droplet of $Ni_{64.7}Fe_{10}Si_{25.3}$ alloy, comprising the regular structure (I) and the refined lamellar structures (II).

Fig. 9. SEM images showing the microstructure of one 75-106 μm droplet of $Ni_{64.7}Fe_{10}Si_{25.3}$ alloy, comprising the regular structure (I) and anomalous structure (III).

Fig. 10. (a) SEM image showing the microsturcture of one 106-150 μm droplet of $Ni_{59.7}Fe_{15}Si_{25.3}$ alloy, consisting of the mixed structure of II and III; (b) micrograph from the region highlighted by the black square.

Fig. 11. SEM images of droplets displaying only the anomalous structure. (a,b): 75-106 μm size fraction, $Ni_{64.7}Fe_{10}Si_{25.3}$ alloy, (c,d): 150-212 μm size fraction, $Ni_{59.7}Fe_{15}Si_{25.3}$ alloy.

Fig. 12. (a) Percentage of the different particle types (A, B or C) as a function of size range in the $Ni_{64.7}Fe_{10}Si_{25.3}$ alloy (solid curves) and $Ni_{59.7}Fe_{15}Si_{25.3}$ alloy (dashed curves). The numbers of the particles counted are also listed in brackets beneath the *x*-coordinate. The numbers of the large particles (>212 μm) have not been counted here as there are no instances of these particles displaying other than Type A characteristics. (b) Estimated volume fraction of $Ni_{25}Si_9$ as a function of particle size in the $Ni_{64.7}Fe_{10}Si_{25.3}$ and $Ni_{59.7}Fe_{15}Si_{25.3}$ alloys.

Fig. 13. SEM image of a particle from the 212-150 μm size range for the $Ni_{64.7}Fe_{10}Si_{25.3}$ alloy, showing the direct transition from structure I to II.

Fig. 14. SEM image of the $Ni_{59.7}Fe_{15}Si_{25.3}$ alloy showing the refined lamellar structure developing on the surface of the γ-$Ni_{31}Si_{12}$ and $Ni_{25}Si_9$ phases.

Fig. 15. EDX determination of the average Fe and Si compositions of the $Ni_{64.7}Fe_{10}Si_{25.3}$ and $Ni_{59.7}Fe_{15}Si_{25.3}$ alloys. Results 1 and 2 are average Si and Fe composition of the particles, while results 3 and 4 are the Si and Fe compositions of the γ phase in the respective particles ranges.

Fig. 16. Microprobe line-scan determination of the composition in the primary γ phase and eutectic regions for two separate particles, both of which are from 150-212 μm size range and are for the $Ni_{59.7}Fe_{15}Si_{25.3}$ alloy.

Fig. 17. TEM high-resolution image of the eutectic structure of the $Ni_{64.7}Fe_{10}Si_{25.3}$ droplet, showing γ-$Ni_{31}Si_{12}$ and $\beta_1(L1_2)$ regions.

Fig. 18. Calculated cooling rate versus droplet diameter during drop-tube processing.

Table 1. Relationship between observed microstructure morphology, constituent phase(s) and droplet classification

Table 2. Parameters used to estimate the cooling rate and undercooling [31-36]

Table 1. Relationship between observed microstructure morphology, constituent phase(s) and droplet classification

<table>
<tr><th>Morphology</th><th>Phase</th><th colspan="2">Droplet Classification</th></tr>
<tr><td>Regular (I)</td><td>Single phase γ-$Ni_{31}Si_{12}$
+
γ-$Ni_{31}Si_{12}$ + β_1-Ni_3Si eutectic</td><td>Type A</td><td rowspan="3">Mixture of I with either/both of II/III

Type B</td></tr>
<tr><td>Refined lamellar (II)</td><td>γ-$Ni_{31}Si_{12}$ + β_1-Ni_3Si eutectic</td><td rowspan="2">Type C</td></tr>
<tr><td>Anomalous (III)</td><td>Single phase$Ni_{25}Si_9$</td></tr>
</table>

Table 2. Parameters used to estimate the cooling rate and undercooling [31-36]

Quantity	value	Unit
Properties of the Gas		
Thermal conductivity, κ_g	0.0249	J m^{-1} s^{-1} K^{-1}
Density, ρ_g	0.561	kg m^{-3}
Dynamic viscosity, η_g	0.0000179	kg m^{-1} s^{-1}
Heat capacity, c_g	1038.310	J kg^{-1} K^{-1}
Mole mass, M	0.028	kg mol^{-1}
Gas constant, R	8.314	J mol^{-1} K^{-1}
Properties of the Alloy		
Mass density, ρ	6.458×10^{3}	kg m^{-3}
Heat capacity, C_p	743.76	J kg^{-1} K^{-1}
Surface emissivity, ε	0.4002	-
Stefan-Boltzmann constant, σ_{SB}	5.67×10^{-8}	W m^{-2} K^{-4}
Relatively drop velocity, V_r	1.0	m s^{-1}
Droplet temperature, T	1600	K
Ambient temperature, T_0	300	K

Figure 1

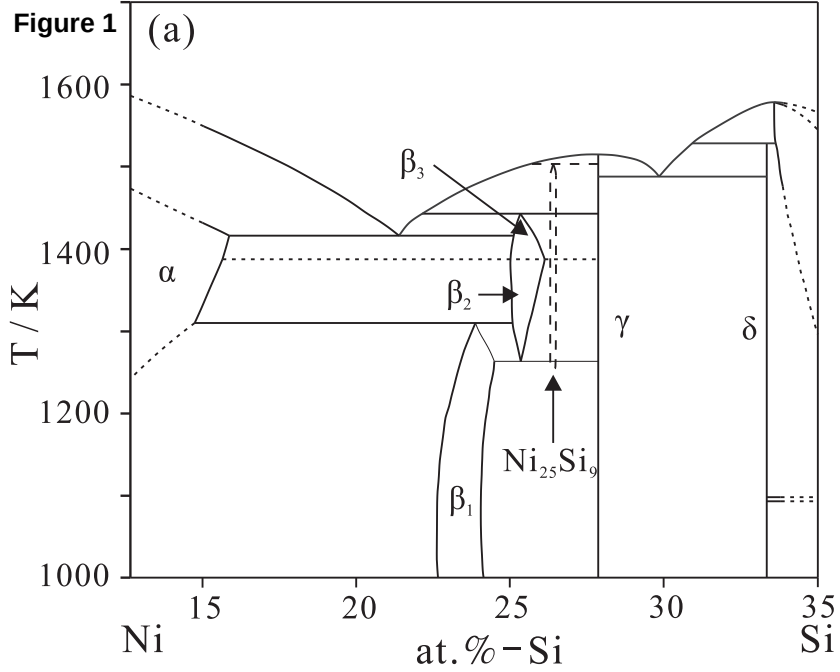
(a)
1600
1400
1200
1000
T / K
β3
α
β2
γ
δ
β1
Ni25Si9
15
20
25
30
35
Ni
at.%−Si
Si

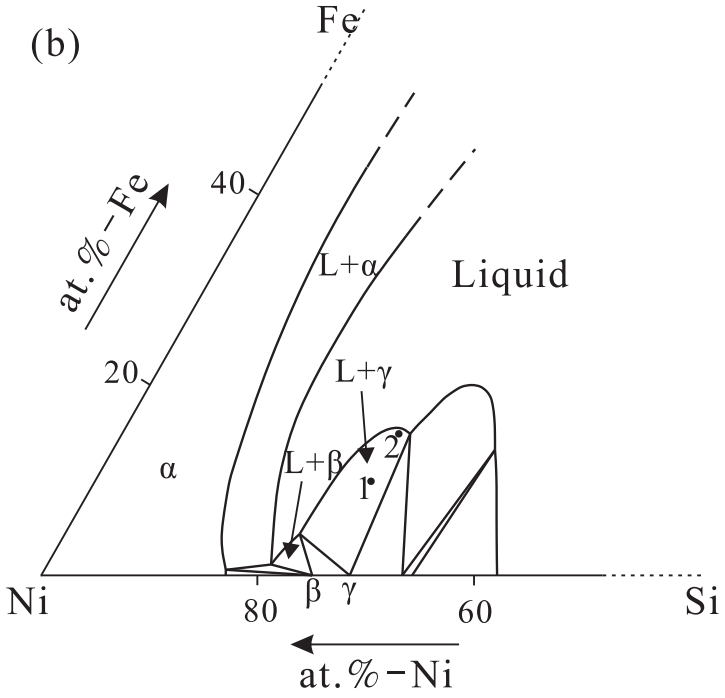
(b)
Fe
40
at.%−Fe
20
L+α
Liquid
L+γ
L+β
2
1
α
Ni
80
β
γ
60
Si
at.%−Ni

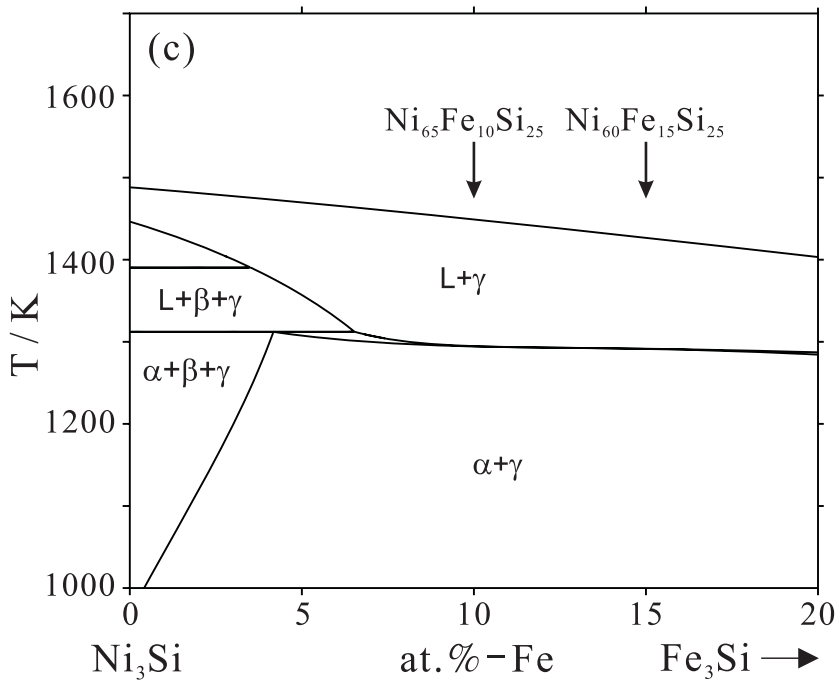
(c)
Ni65Fe10Si25
Ni60Fe15Si25
1600
1400
1200
1000
T / K
L+γ
L+β+γ
α+β+γ
α+γ
0
5
10
15
20
Ni3Si
at.%−Fe
Fe3Si

Figure 2

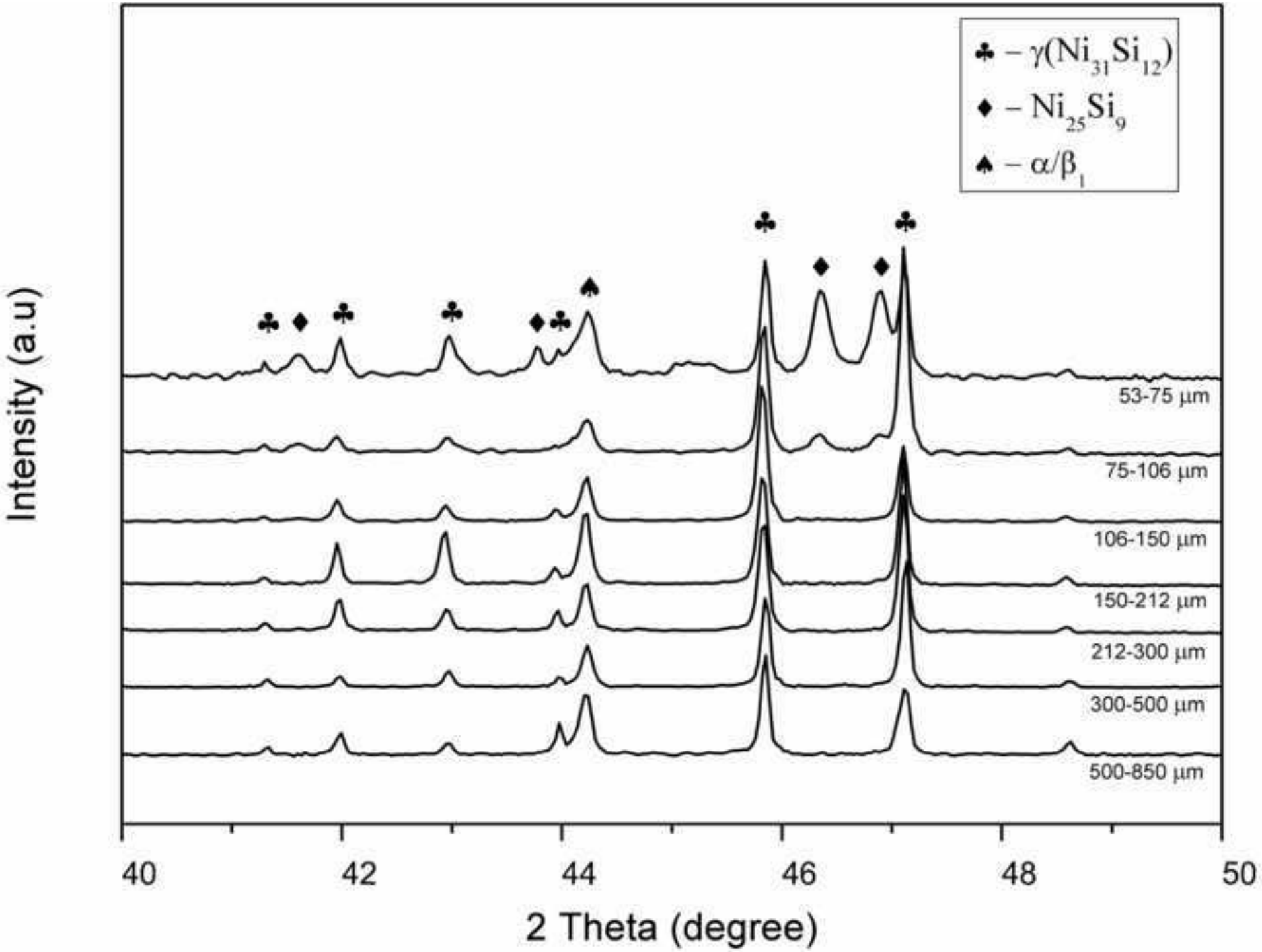
♣ – γ(Ni31Si12)
♦ – Ni25Si9
♠ – α/β1
53-75 μm
75-106 μm
106-150 μm
150-212 μm
212-300 μm
300-500 μm
500-850 μm
Intensity (a.u)
40
42
44
46
48
50
2 Theta (degree)

Figure 3

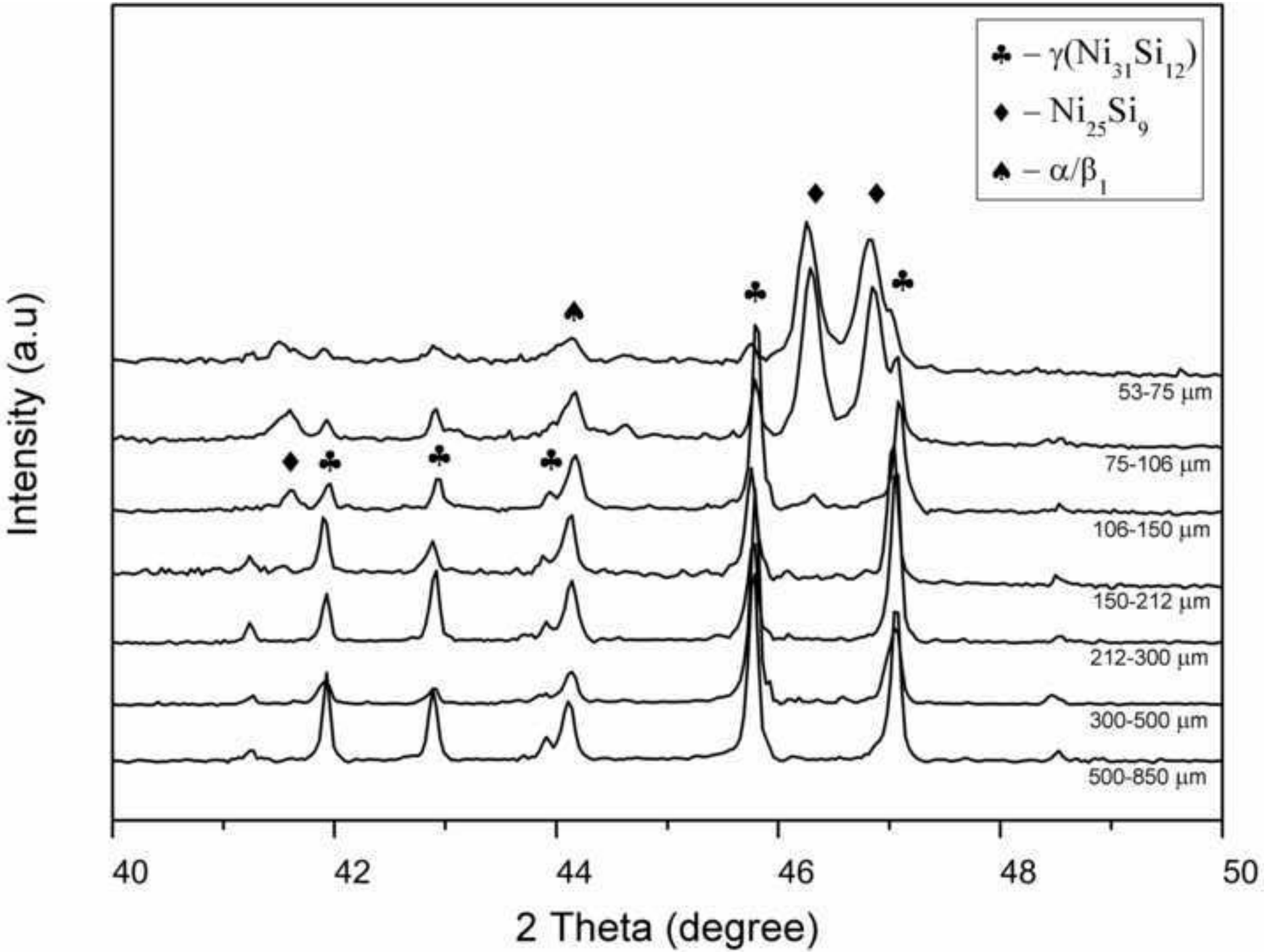
♣ – γ(Ni31Si12)
♦ – Ni25Si9
♠ – α/β1
53-75 μm
75-106 μm
106-150 μm
150-212 μm
212-300 μm
300-500 μm
500-850 μm
Intensity (a.u)
40
42
44
46
48
50
2 Theta (degree)

Figure 4

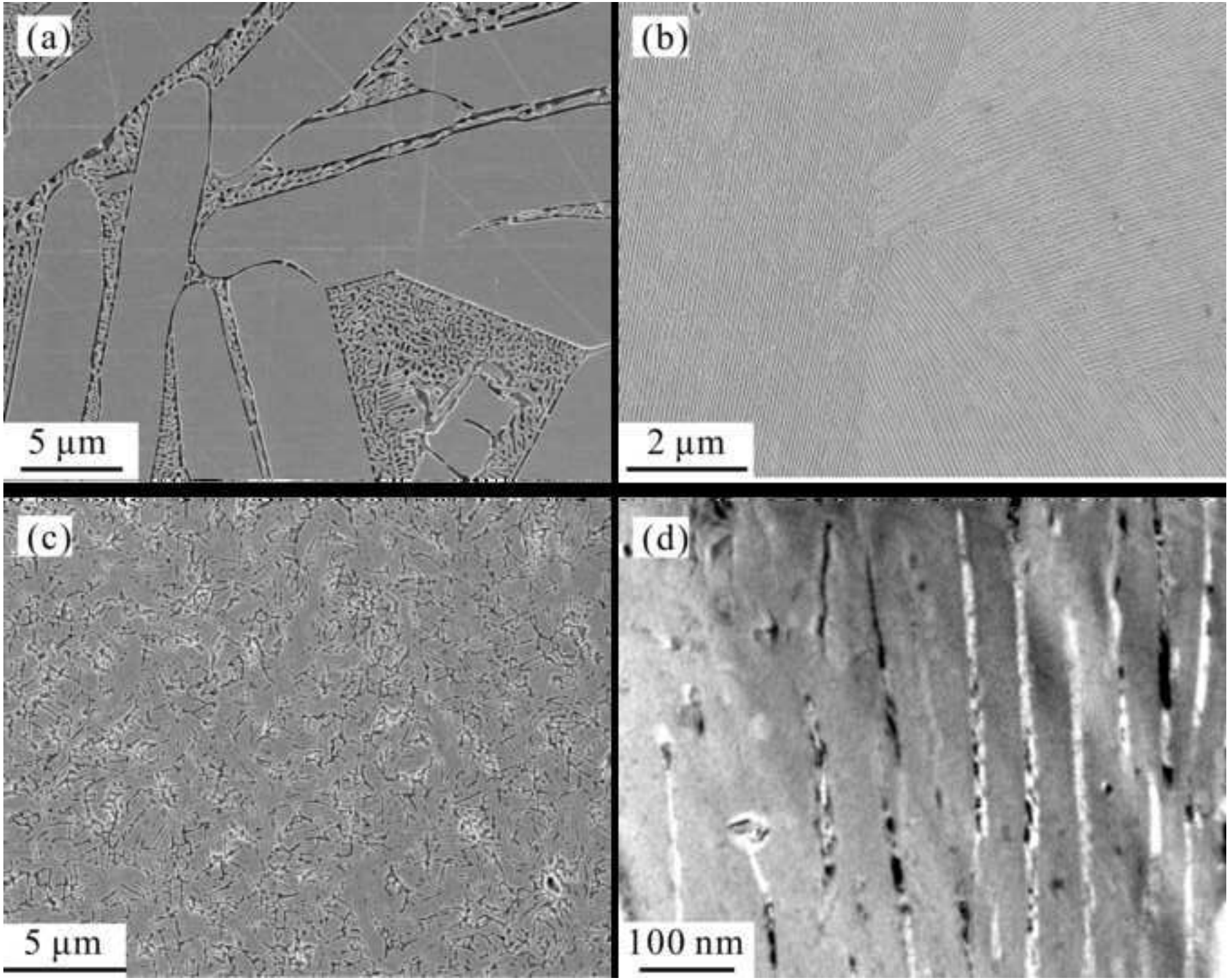

Figure 5

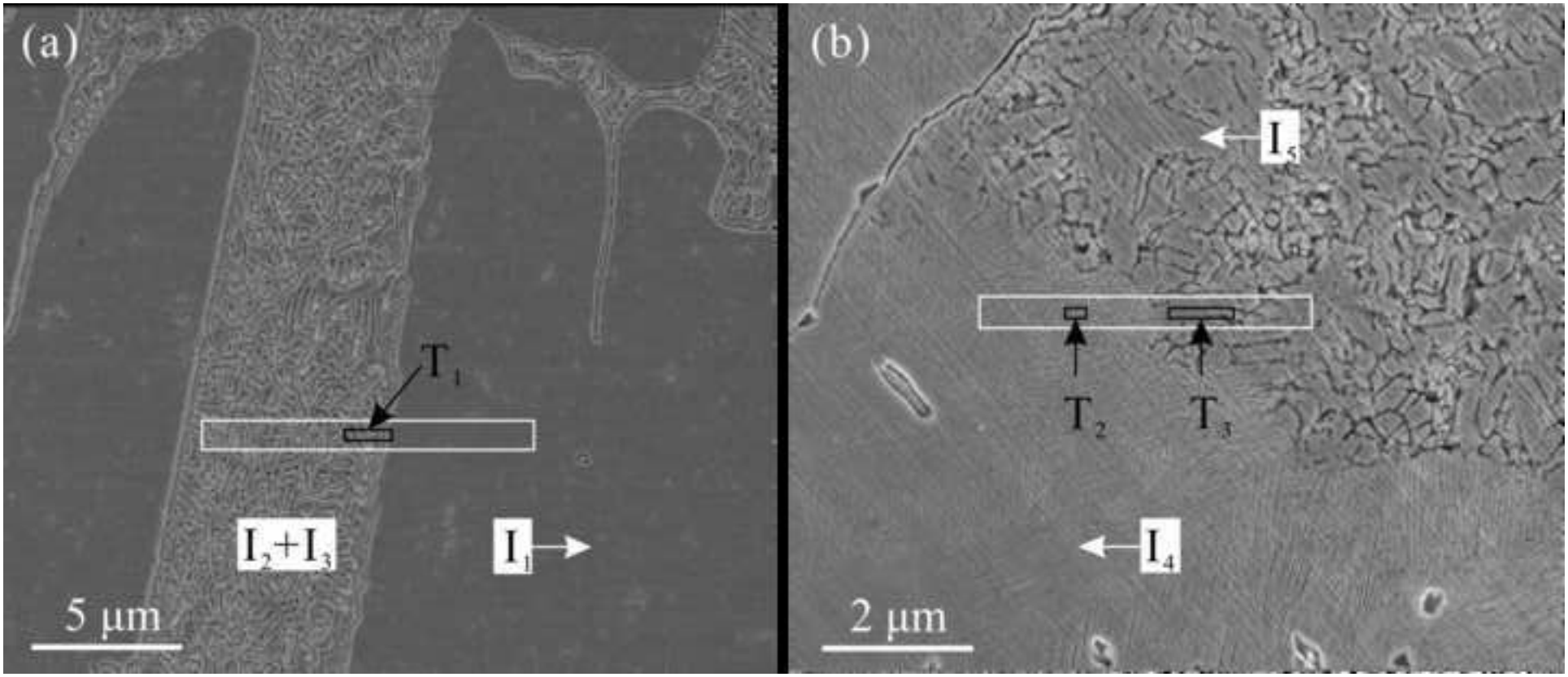

Figure 6

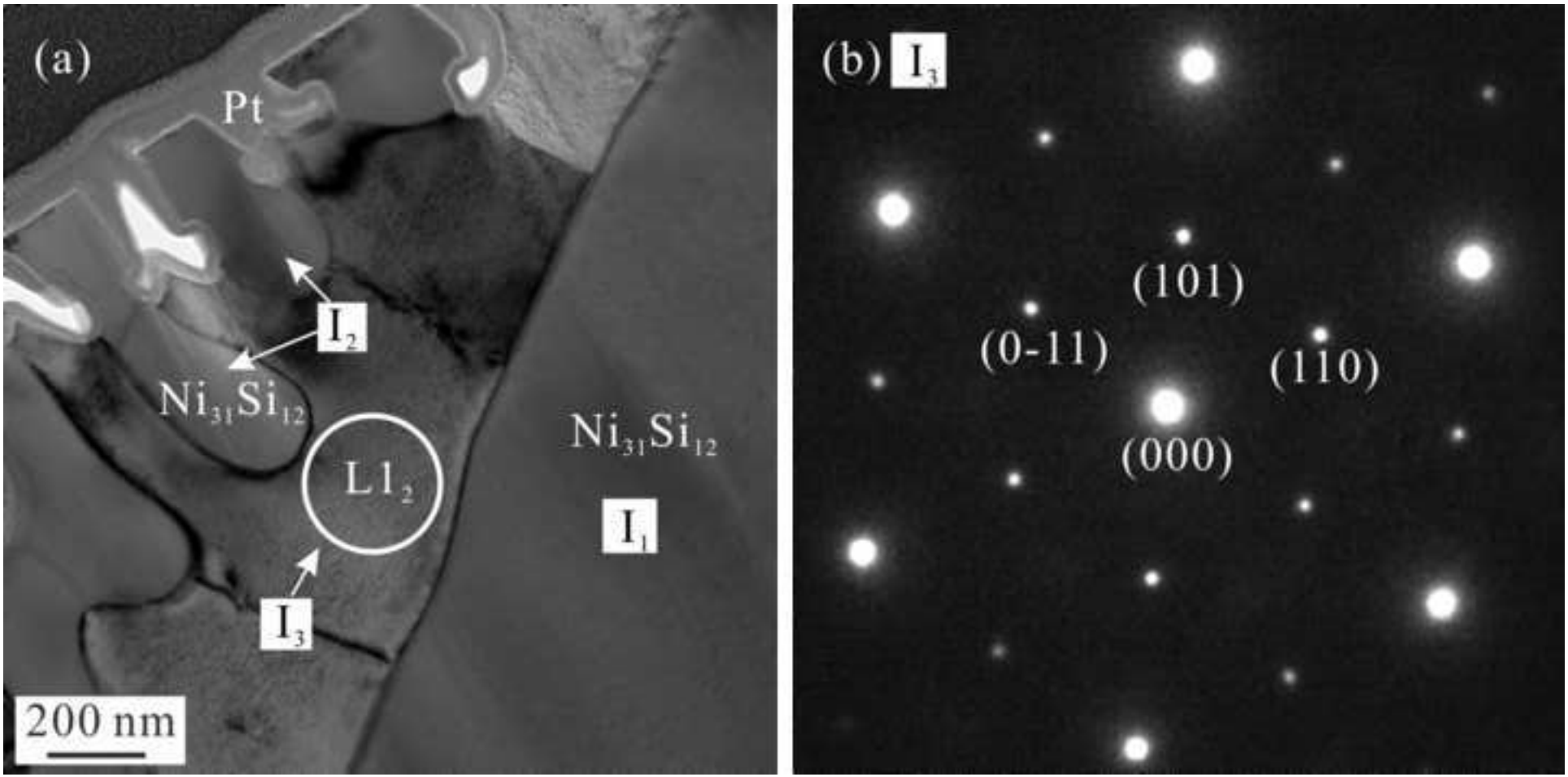

Figure 7

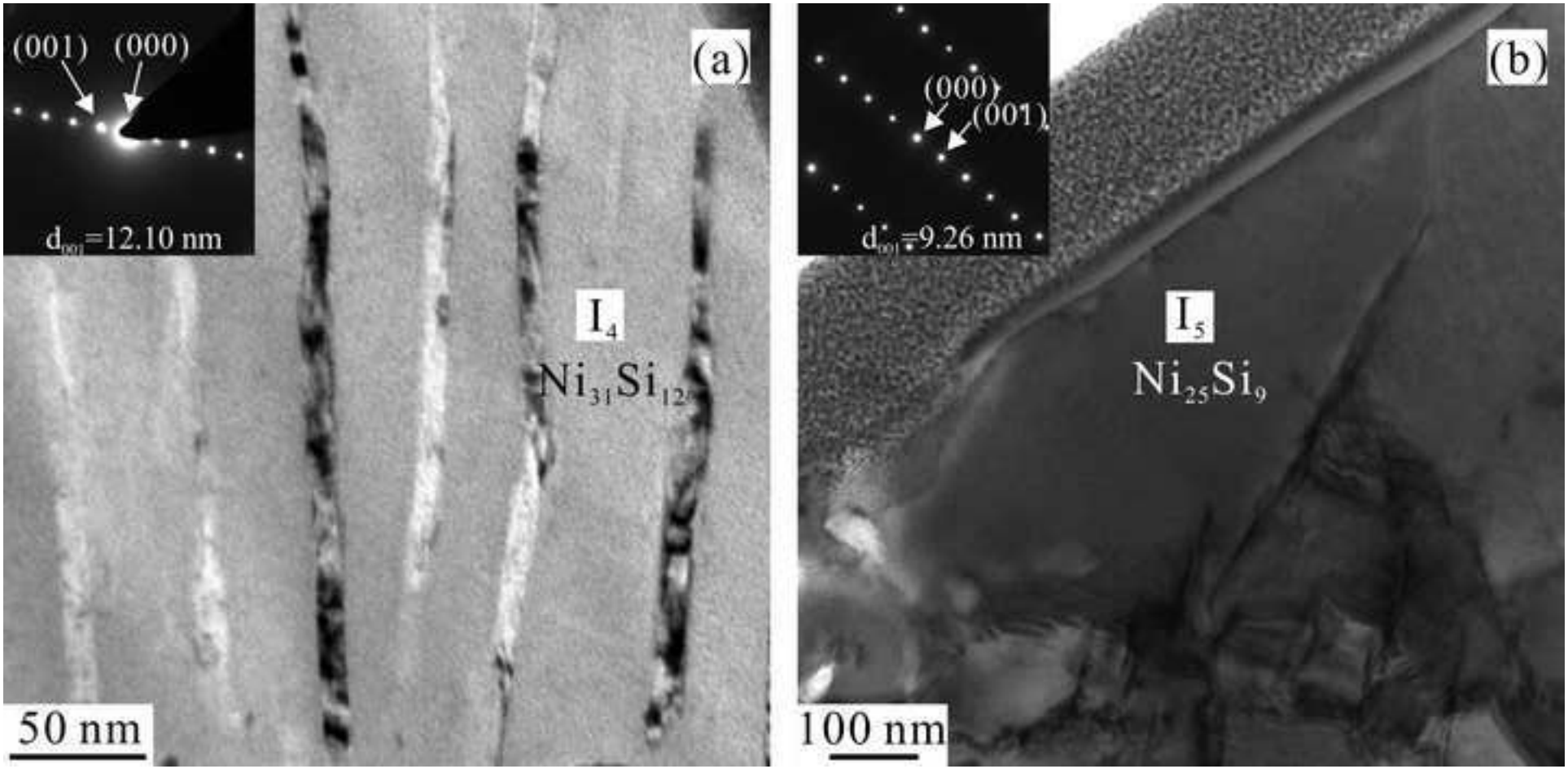
(001)
(000)
d_{001}=12.10 nm
(a)
I_4
$Ni_{31}Si_{12}$
50 nm
(000)
(001)
d_{001}=9.26 nm
(b)
I_5
$Ni_{25}Si_9$
100 nm

Figure 8

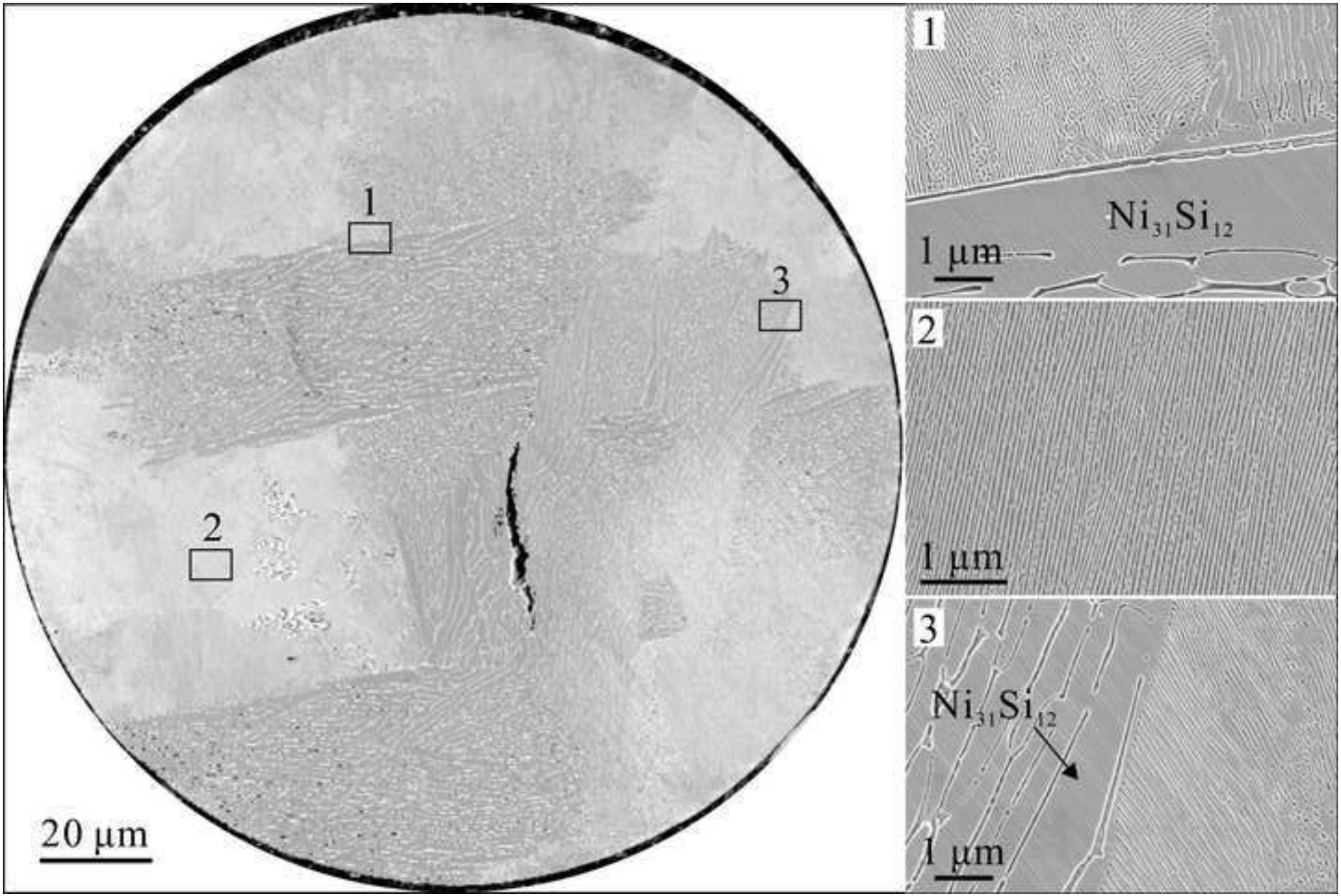

Figure 9

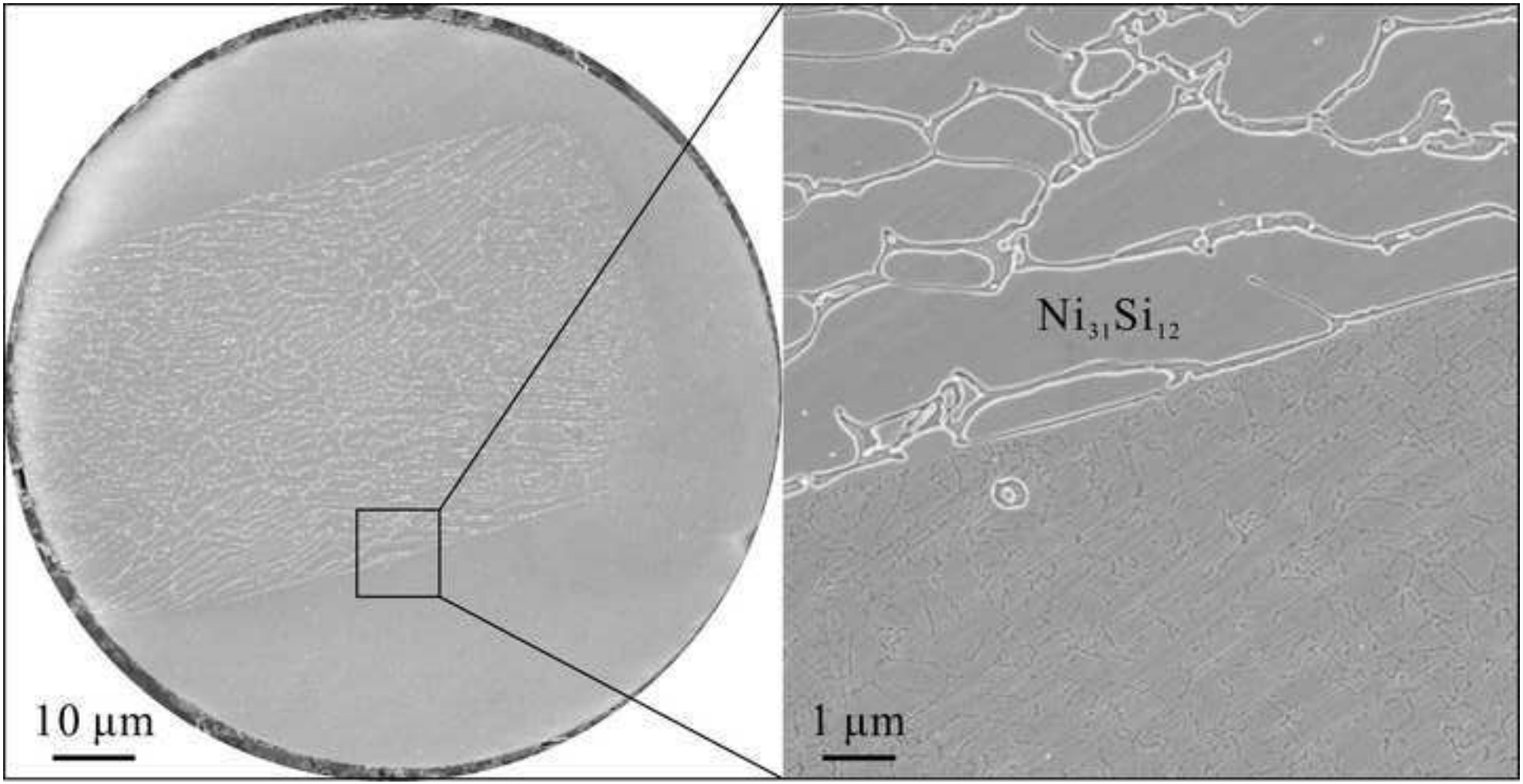

Figure 10

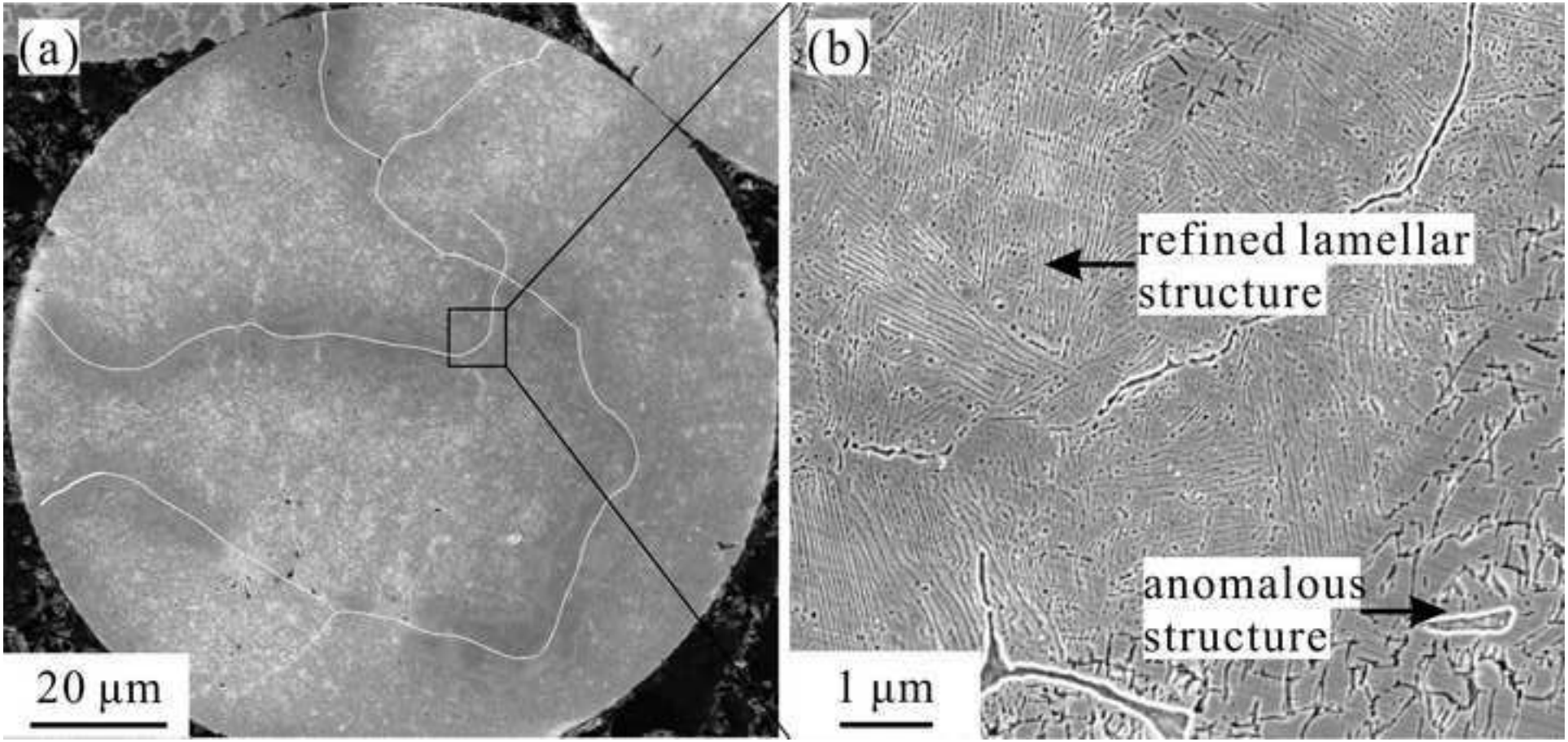
(a)
20 μm
(b)
refined lamellar structure
anomalous structure
1 μm

Figure 11

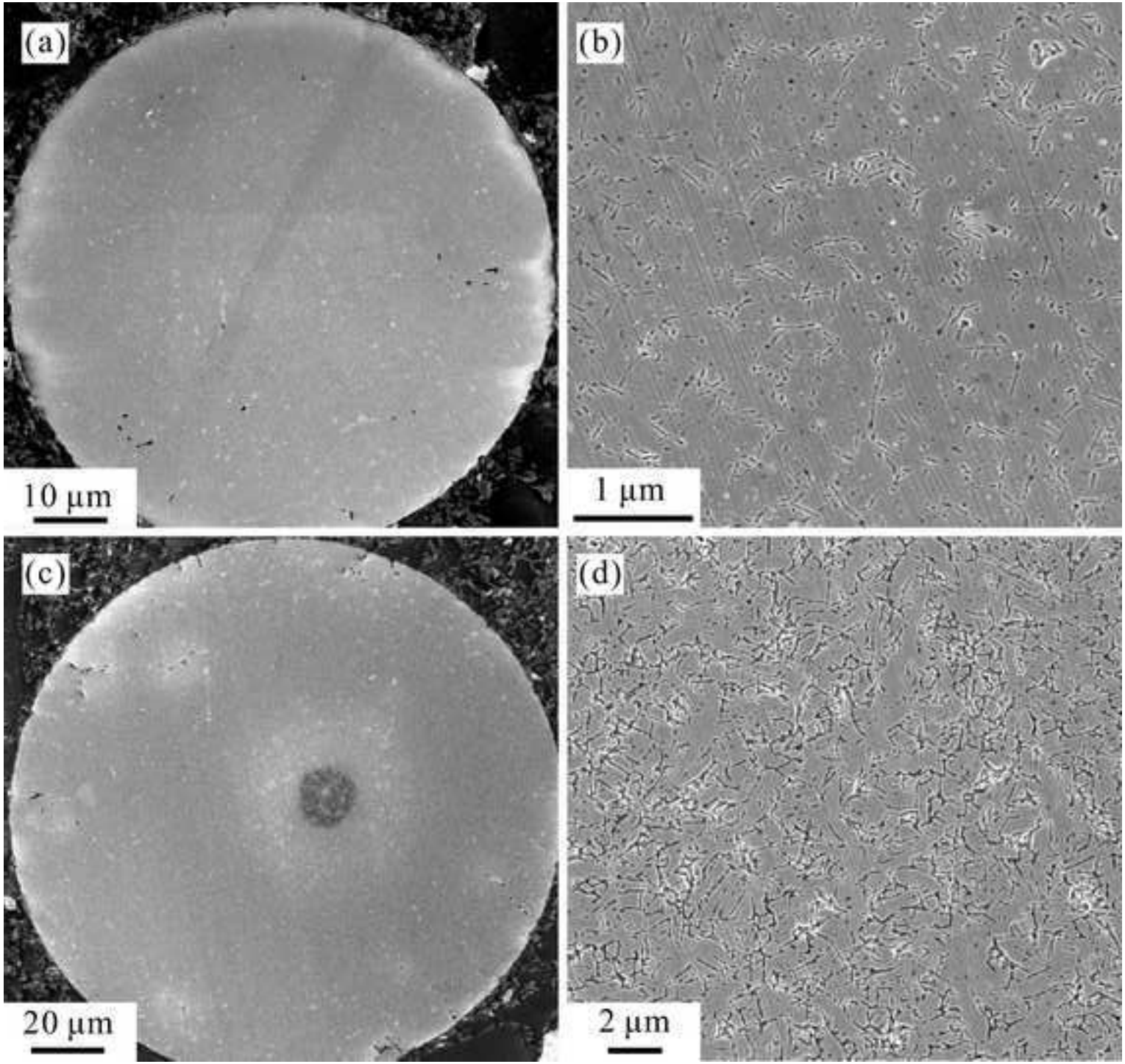

Figure 12

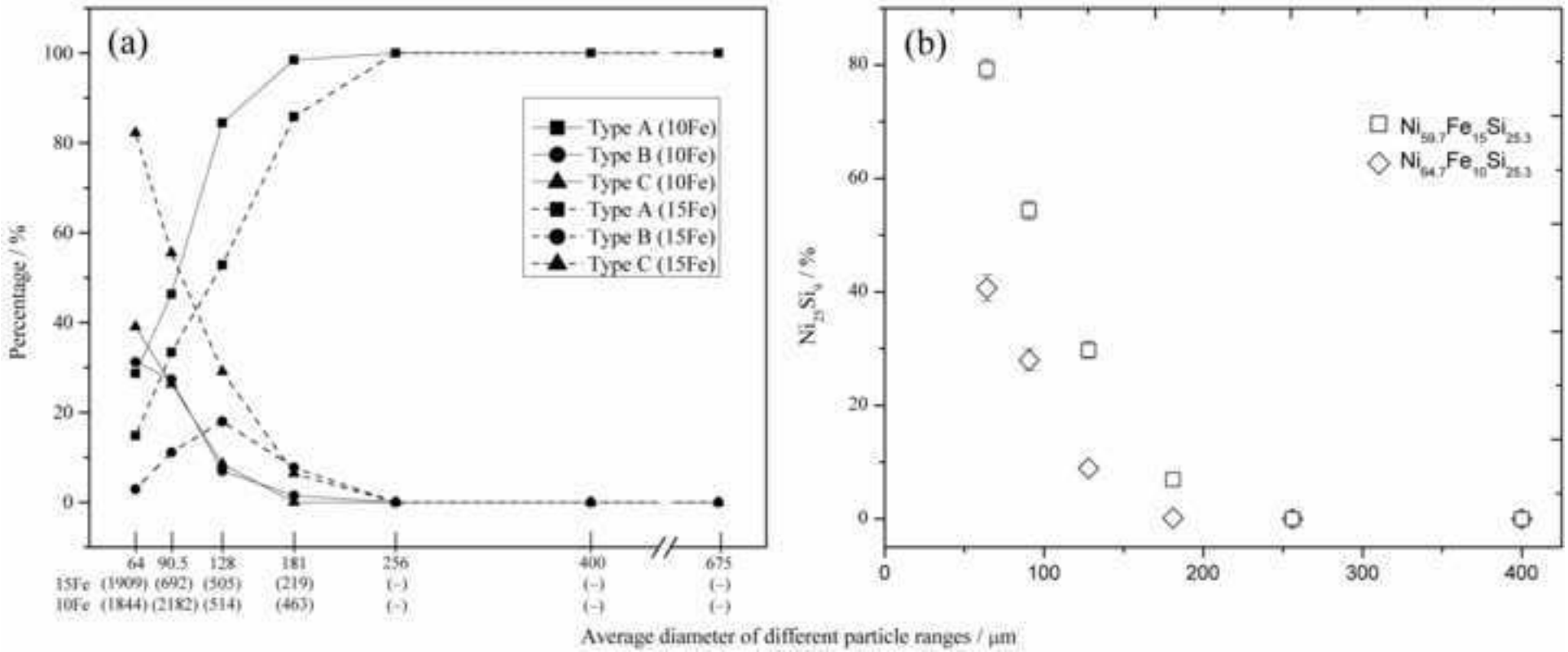
(a)
Percentage / %
Type A (10Fe)
Type B (10Fe)
Type C (10Fe)
Type A (15Fe)
Type B (15Fe)
Type C (15Fe)
64 90.5 128 181 256 400 675
15Fe (1909) (692) (505) (219) (–) (–) (–)
10Fe (1844) (2182) (514) (463) (–) (–) (–)
(b)
$Ni_{25}Si_9$ / %
$Ni_{59.7}Fe_{15}Si_{25.3}$
$Ni_{64.7}Fe_{10}Si_{25.3}$
Average diameter of different particle ranges / μm

Figure 13

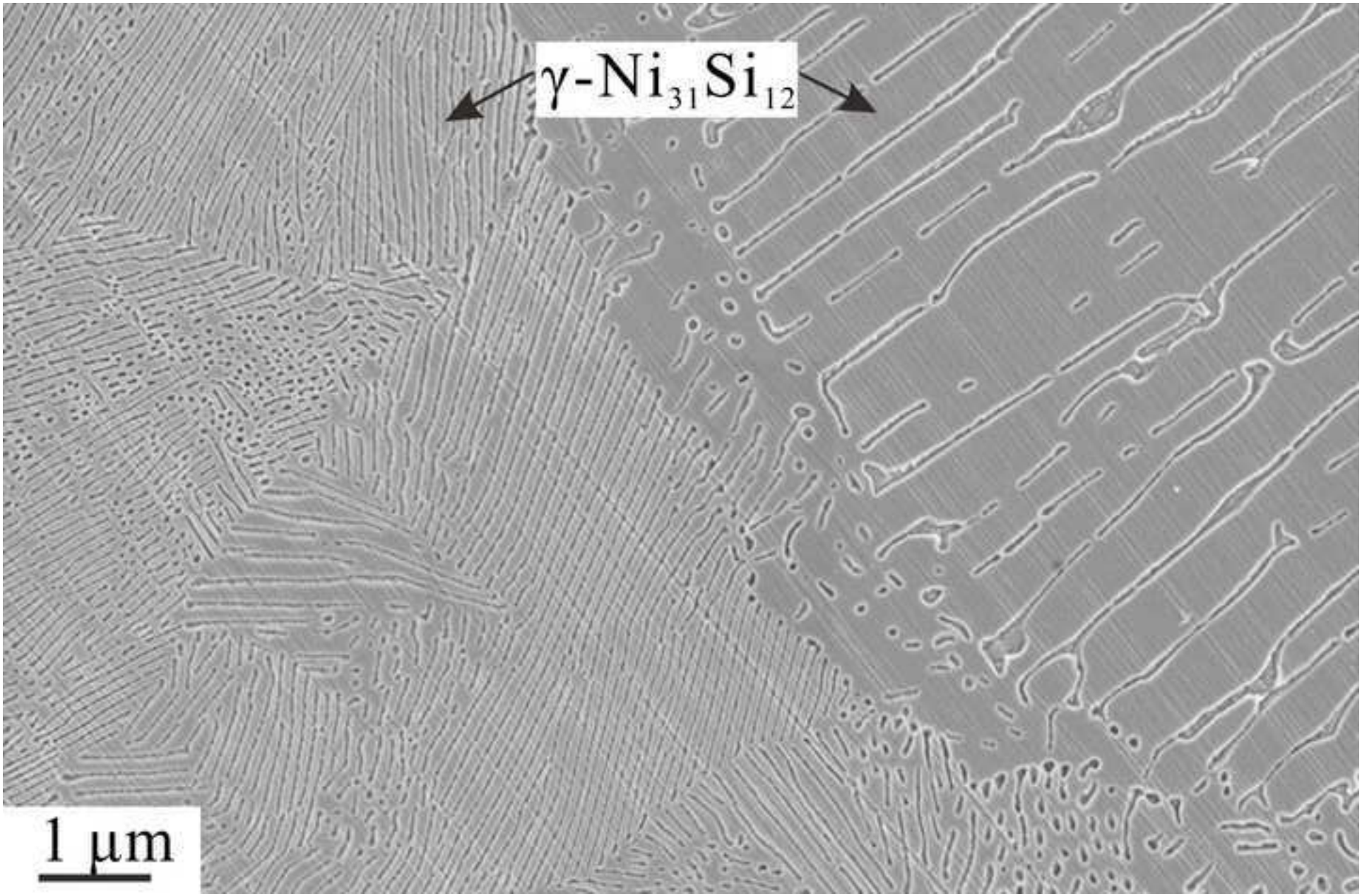

Figure 14

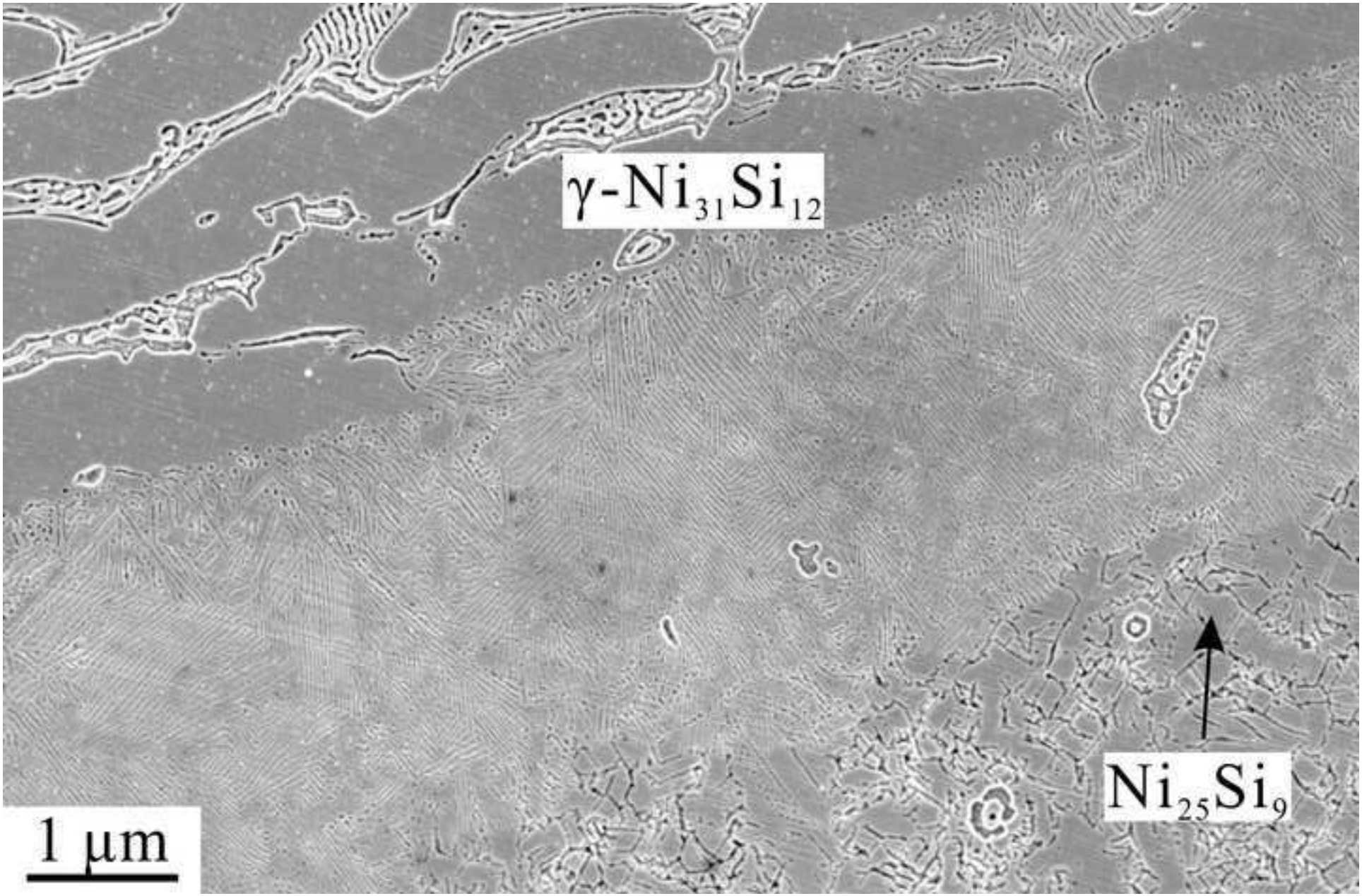

Figure 15

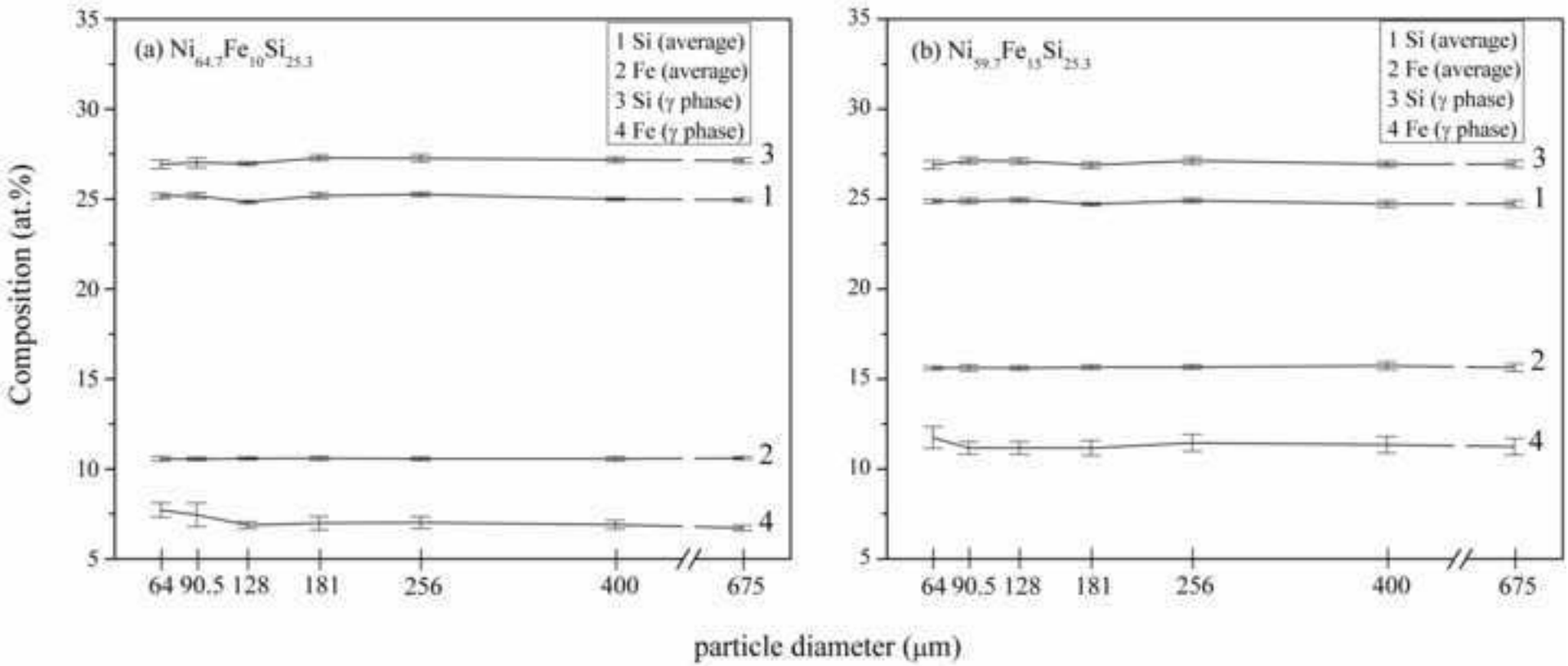
(a) Ni64.7Fe10Si25.3
(b) Ni59.7Fe15Si25.3
1 Si (average)
2 Fe (average)
3 Si (γ phase)
4 Fe (γ phase)
Composition (at.%)
particle diameter (μm)
35
30
25
20
15
10
5
64
90.5
128
181
256
400
675
1
2
3
4

Figure 16

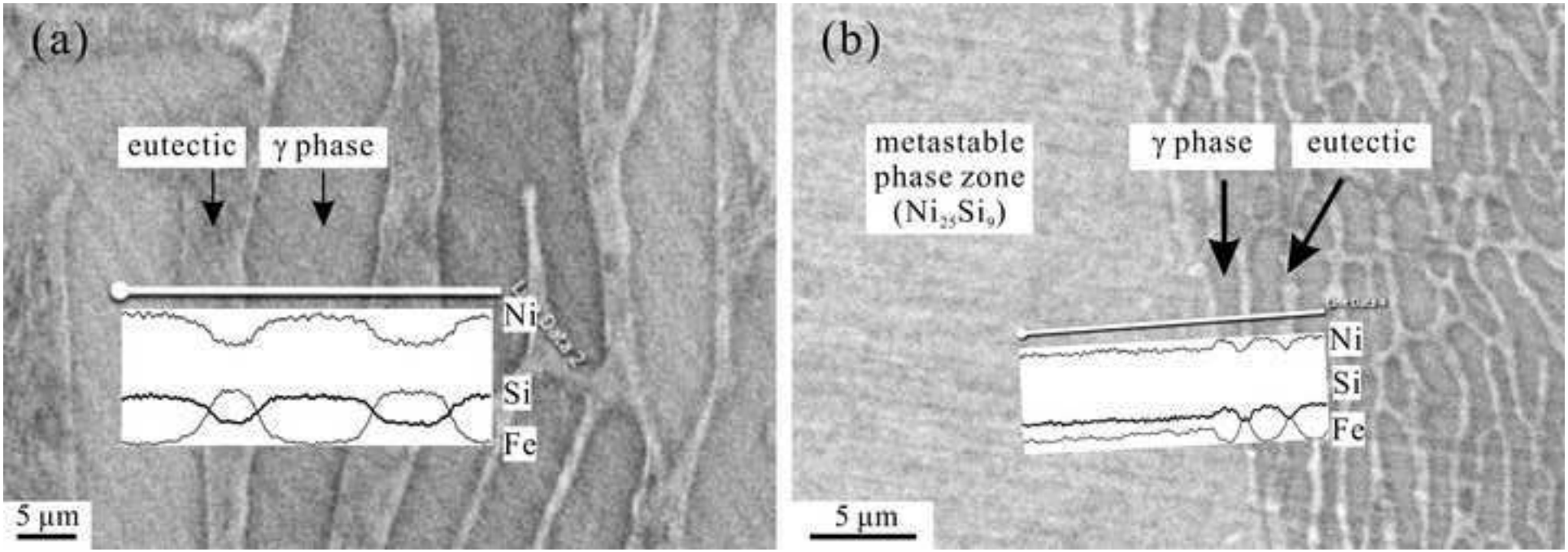
(a)
eutectic
γ phase
Ni
Si
Fe
5 μm
(b)
metastable
phase zone
(Ni25Si9)
γ phase
eutectic
Ni
Si
Fe
5 μm

Figure 17

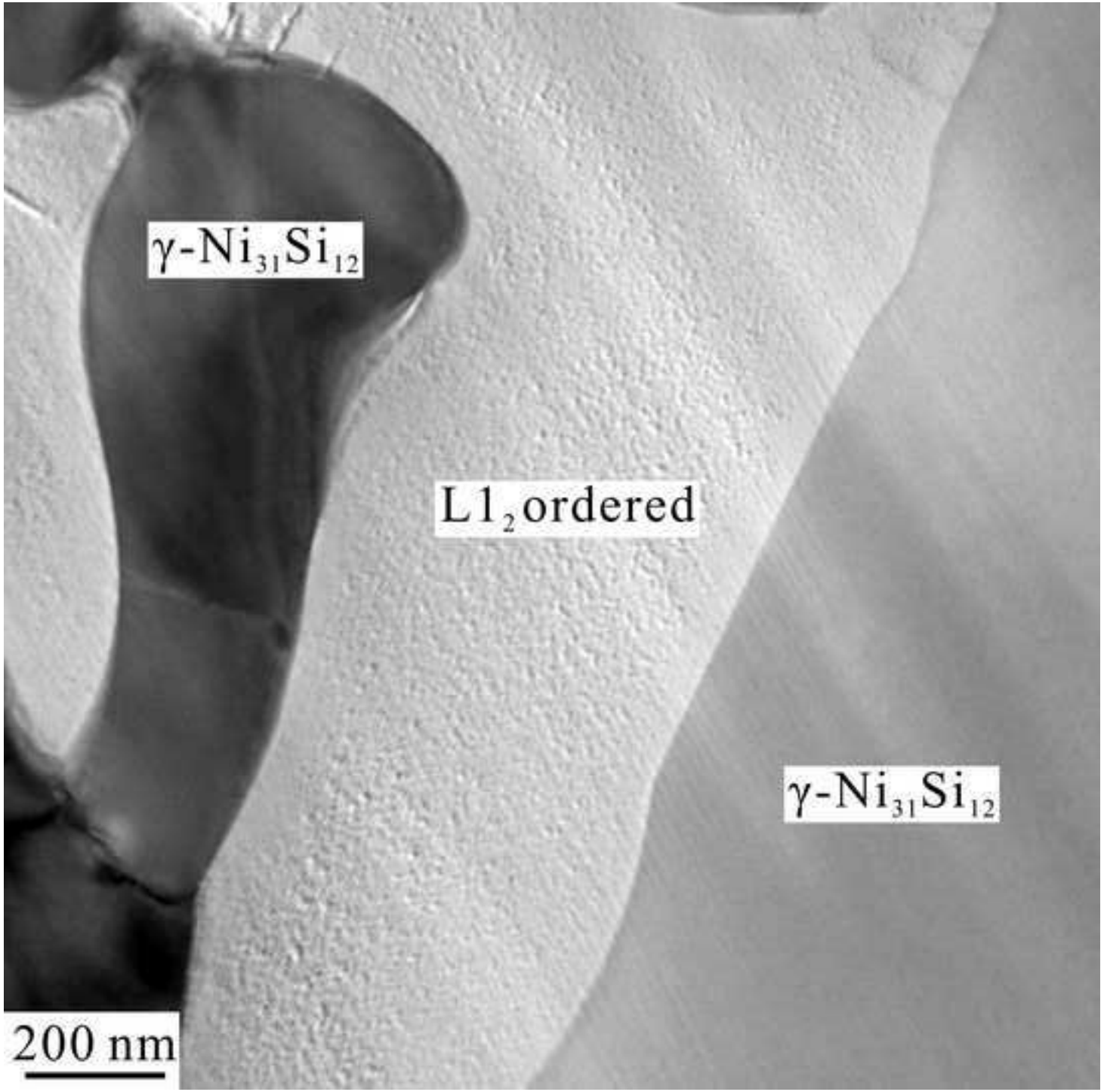

Figure 18

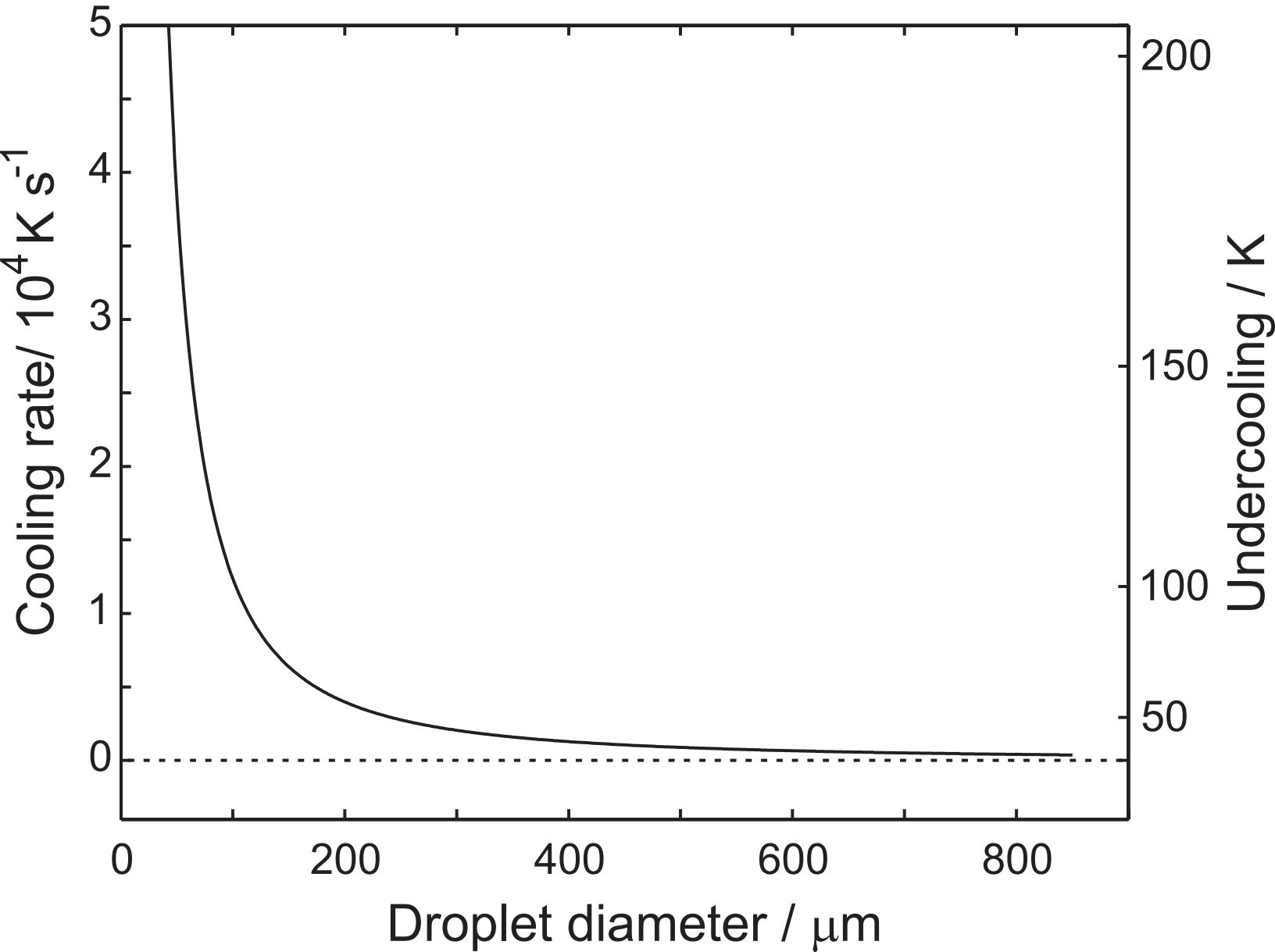
Cooling rate/ 10^4 K s^-1
Undercooling / K
Droplet diameter / μm
0
1
2
3
4
5
50
100
150
200
0
200
400
600
800